universe

IMPACT FACTOR 2.5

CITESCORE 4.3

Article

Isospin QCD as a Laboratory for Dense QCD

Toru Kojo, Daiki Suenaga and Ryuji Chiba

Special Issue
Studies in Neutron Stars

Edited by
Dr. Ana Gabriela Grunfeld and Prof. Dr. David Blaschke

MDPI

https://doi.org/10.3390/universe10070293

universe

MDPI

Article

Isospin QCD as a Laboratory for Dense QCD

Toru Kojo [1,*], Daiki Suenaga [2,3] and Ryuji Chiba [1]

[1] Department of Physics, Tohoku University, Sendai 980-8578, Japan
[2] Kobayashi-Maskawa Institute for the Origin of Particles and the Universe, Nagoya University, Nagoya 464-8602, Japan
[3] Research Center for Nuclear Physics, Osaka University, Ibaraki 567-0048, Japan
* Correspondence: toru.kojo.b1@tohoku.ac.jp

Abstract: QCD with the isospin chemical potential μ_I is a useful laboratory to delineate the microphysics in dense QCD. To study the quark–hadron continuity, we use a quark–meson model that interpolates hadronic and quark matter physics at microscopic level. The equation of state is dominated by mesons at low density but taken over by quarks at high density. We extend our previous studies with two flavors to the three-flavor case to study the impact of the strangeness, which may be brought by kaons $(K_+, K_0) = (u\bar{s}, s\bar{d})$ and the $U_A(1)$ anomaly. In the normal phase, the excitation energies of kaons are reduced by μ_I in the same way as hyperons in nuclear matter at the finite baryon chemical potential. Once pions condense, kaon excitation energies increase as μ_I does. Moreover, strange quarks become more massive through the $U_A(1)$ coupling to the condensed pions. Hence, at zero and low temperature, the strange hadrons and quarks are highly suppressed. The previous findings in two-flavor models, sound speed peak, negative trace anomaly, gaps insensitive to μ_I, persist in our three-flavor model and remain consistent with the lattice results to $\mu_I \sim 1$ GeV. We discuss the non-perturbative power corrections and quark saturation effects as important ingredients to understand the crossover equations of state measured on the lattice.

Keywords: equations of state; pion condensation; quark–hadron continuity; power corrections; quark saturation

Citation: Kojo, T.; Suenaga, D.; Chiba, R. Isospin QCD as a Laboratory for Dense QCD. *Universe* **2024**, *10*, 293. https://doi.org/10.3390/universe10070293

Academic Editors: Ana Gabriela Grunfeld and David Blaschke

Received: 16 June 2024
Revised: 6 July 2024
Accepted: 10 July 2024
Published: 12 July 2024

1. Introduction

Recently there has been increasing attention paid to two-color QCD (QC_2D) [1–19], or QCD at finite isospin but zero baryon densities (isospin QCD, QCD_I in short) [20–31]. In these theories, lattice simulations are viable without the sign problem. Confronting theories with lattice results should provide us with useful insights into QCD matter at high baryon density (n_B); see, for example, reviews [32–36].

Equations of state (EOSs) of dense matter have a one-to-one correspondence with the mass-radius (M-R) relations of neutron stars. One of the important indications from neutron star observations and nuclear constraints is that QCD matter is soft around nuclear saturation density $n_0 \simeq 0.16\,\mathrm{fm}^{-3}$, but rapidly becomes stiff around $n_B = 2$–$4n_0$ [37,38]. The density for this radical stiffening is smaller than the density where baryons of the radius 0.5–0.8 fm spatially overlap. Meanwhile nuclear many-body calculations become problematic for $n_B \gtrsim 1.5$–$2n_0$. Observationally, rapid stiffening is supported by a small variation (or even increase) in radii from $1.4M_\odot$ to $2.1M_\odot$ neutron stars. If EOSs stiffen only gently as in typical hadronic EOS with many-body forces, the radii of $\simeq 2M_\odot$ neutron stars would be substantially smaller than $1.4M_\odot$ neutron stars by $\sim$1 km [39]. Such contrast in $1.4M_\odot$ to $2.1M_\odot$ radii may be also studied by gravitational waves from binary neutron star mergers; see, for example, Refs. [40–43].

To study the interplay between hadronic and quark matter, it is crucial to understand rapid stiffening at the microscopic level. Several theoretical studies [44–47] suggest that such rapid stiffening around 2–$4n_0$ is triggered by quark degrees of freedom, whether

or not quarks are confined or deconfined. Assuming a model in which quarks remain confined in baryons, quarks can still occupy states with a certain probability and eventually affect baryons through the quark Pauli blocking [46,47]. Such quark constraint becomes substantial even before baryons overlap. After quark states at low momentum are saturated ("quark saturation" [46]), the quark Fermi sea begins to form with the diffused Fermi surface whose thickness is $\simeq$200–300 MeV. The quark saturation forces matter of non-relativistic baryons to change into that of relativistic baryons or quarks, driving the rapid growth in pressure but modest change in the energy density [46]. The quark momentum distribution at finite density has been manifestly computed for two-dimensional QCD [48].

The quark saturation and the associated stiffening may occur also in $\mathrm{QC_2D}$ and QCD_I, although baryons are replaced with diquark baryons and mesons, respectively. In these theories, the Bose–Einstein Condensation of diquarks or mesons occurs at the onset of matter; (composite) bosons occupy the zero momentum state. At a finite chemical potential exceeding the mass threshold, the amplitude of condensates would grow indefinitely unless some sort of repulsive forces temper the growth of the amplitude. For theories of elementary bosons, we do not have definite rationals why such repulsion should exist, while, for theories of bosons made of fermions, the indefinite growth in boson amplitudes would violate the Pauli exclusion principle. Hence, irrespective to the details of interactions, effective repulsions among bosons must emerge.

For isospin QCD, there have been many studies; see Ref. [49] for a recent good summary to 2019. Recently, isospin QCD has attracted renewed attention as a laboratory to study concepts proposed for neutron star physics [50–52] or to derive some constraints on neutron star EOS [53–56]. In Refs. [50,51], we used a two-flavor quark–meson model to discuss the rapid stiffening and related microphysics. This model is renormalizable and includes mesons and quarks [57,58]. At low density, the EOS is dominated by mesons while, at high density, quarks dominate. In quark matter, region mesonic degrees of freedom as condensates remain near the quark Fermi surface.

In this paper, after adding some supplements to our previous two-flavor studies, we then extend the analyses to three flavors. Although a strange quark does not have isospin, hadronic strange particles, such as kaons, η, η', and so on, contain u,d-quarks and can be affected by the isospin density. Indeed, the excitation energies of $(K_+, K_0) = (u\bar{s}, s\bar{d})$ decrease with increasing μ_I and would eventually condense unless other particles in the system repel such kaons. Another effect of interest is the impact of the $\mathrm{U}_A(1)$ anomaly that affects the strangeness in the Dirac sea [59,60]. At finite density, the reduction in the effective u,d quark masses softens the chiral symmetry breaking in the strange quark sector, while the appearance of the pion condensates can enhance the strange quark mass by a few hundred MeV. This continues until the medium screening cuts off such effects. A similar coupling, diquark-to-chiral order parameters, has been discussed in the context of quark–hadron crossover [61–64]. Thus, the strange particles are useful probes to diagnose various medium effects in dense matter.

In this paper, we use a quark–meson model to discuss a quark–hadron crossover [65–70]. In Section 2, we first discuss a picture behind this model to inform readers of what physics we try to describe. We will use the $1/N_\mathrm{c}$ expansion to classify the effects caused by different degrees of freedom [71,72]. In Section 3, we present a quark–meson model including the strangeness and the $\mathrm{U}_A(1)$ anomaly effects. In Section 4, we study the effective potential and meson spectra at the tree level. In Section 5, we include quarks to change the structure of the theory and discuss how it leads to the trend consistent with the lattice results. In Section 6, we mention our parameter fixing through meson poles in vacuum with quark-loop corrections. In Section 7, we examine EOS at zero temperature and its relationship with the microphysics. Section 8 is devoted to the summary.

2. A Quark–Meson Model at Finite Density: Outline

We begin with the N_c counting of a quark–meson coupling. A diagrammatic representation is given in Figure 1. To derive the N_c counting of hadronic parameters, we

match the N_c counting in a color line graph and a hadronic graph. For instance, from a mesonic correlator with the magnitude of N_c, one can conclude that a quark bilinear operator couples to a mesonic state with the strength $N_c^{1/2}$. Using this estimate and repeating the similar matching, one can deduce that the meson–meson interaction is $\sim N_c^{-1/2}$ for three-meson vertices and $\sim N_c^{-1}$ for four-meson vertices, and so on. Similarly, for a quark–meson coupling graph with the amplitude of $\sim g_s^2 N_c \sim N_c^0$, one can conclude that the quark–meson coupling is $N_c^{-1/2}$. While we consider only a single gluon exchange, including more gluons introduces $(g_s^2 N_c)^n \sim 1$ so that the counting is not affected.

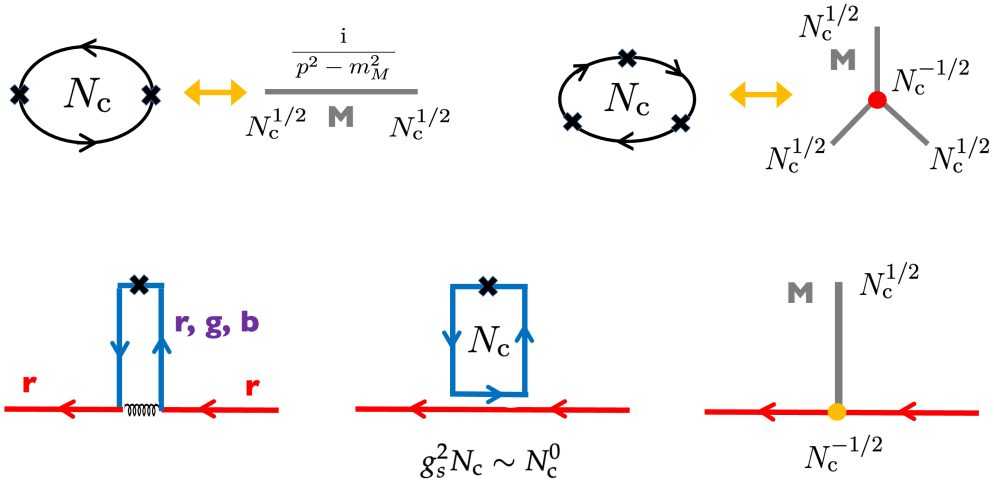

Figure 1. (**upper**) Some examples of the correspondence between quark–gluon, color line graphs, and hadronic graphs. The coupling between quark bilinear operators and mesonic state must be $\sim N_c^{1/2}$ for the consistency with the color line graphs. Meson three-point vertices must be $\sim N_c^{-1/2}$. (**lower**) The quark–meson vertices in quark–gluon, color line, and quark–meson representations. The quark–meson coupling must be $\sim N_c^{-1/2}$ to be consistent with the color line representation.

Below, we assume that this quark–meson coupling g is dominated by soft gluons for which the quark–gluon coupling g_s is large and characterizes the size of the quark–meson coupling. The soft gluon exchanges occur indefinitely within the produced mesons. This sort of process cannot be represented by perturbative treatments at the finite order. The purpose of manifestly including mesonic degrees of freedom is to replace or parametrize these processes in a book keeping manner.

The quark self-energy with gluon loops (leftmost panel, Figure 2) are $g_s^2 N_c \sim N_c^0$ yielding the mass of $\sim \Lambda_{\rm QCD}$. The factor N_c amplification occurs, as there is a color loop in the color line representations. In contrast, the self-energy with mesonic loops is $g^2 \sim g_s^4 N_c \sim N_c^{-1}$ and suppressed (rightmost panel, Figure 2). There is an exception, however. When mesons form condensates, the self-energies originating from meson loops can be amplified to N_c^0. The condensate contains indefinite numbers of $q\bar{q}$ pairs. In the case of chiral condensates, condensed $\bar{q}_L q_R$ or $\bar{q}_R q_L$ pairs transform $q_L(q_R)$ into $q_R(q_L)$, generating the mass self-energies. If we neglect changes in the number of $\bar{q}q$ pairs in the condensate, a quark propagator with meson loops can be factorized into a product of quark propagators with a background meson condensate. Since quark propagators with the meson background already contain graphs with many soft gluons, to avoid double counting, we do not manifestly include the quark self-energy graphs with soft gluon loops. Meanwhile, graphs with hard gluons may be added separately for more complete exploration of the phase space in the intermediate states.

The reduction in meson masses can be important even before mesons condense. Such precursory effects are important near the phase boundaries and have been studied in the context of color superconductivity [73–75].

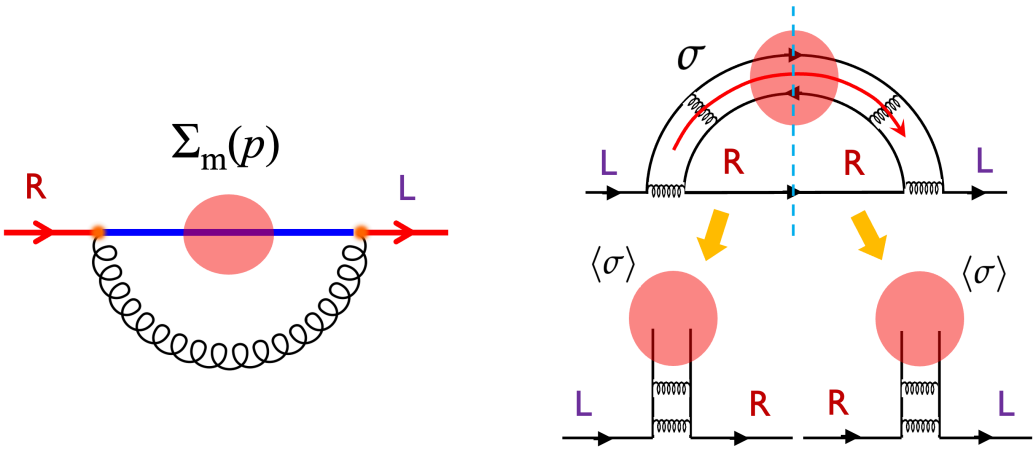

Figure 2. The mass self-energy graphs with (**left**) gluon and (**right**) meson loops. The gluon loop graph is $\sim g_s^2 N_c \sim N_c^0$. The meson loop graph is $\sim g^2 \sim g_s^4 N_c \sim N_c^{-1}$, except when the meson condenses. With meson condensates of $\langle\sigma\rangle \sim f_\pi \sim N_c^{1/2}$, the graphs with condensate can represent (some part of) the gluon loop graphs in the leftmost panel.

We include "mesons" as a representative of the $q\bar{q}$ propagating graph with an indefinite numbers of soft gluon exchanges. Using meson degrees of freedom at high density might look unnatural, but models manifestly including mesons can be dynamical reduced to pure quark descriptions; the dissociation and structural changes of these mesons into quarks can be described by inserting quark loops in the meson propagators. Thus, unwanted contributions can be canceled by including quark loops [76].

At high density, quarks typically have large momenta, but the excitation energies can be small, $\sim E - \mu \ll \mu$ (μ: chemical potential) near the Fermi surface. These soft quarks and soft gluons may keep quark–meson couplings as strong as in vacuum unless screening processes cut off soft gluons. For S-wave condensates, a quark with $\vec{p}$ and an antiquark with $-\vec{p}$ make a pair in which soft gluons are exchanged. For a pion-condensed phase in isospin QCD, these soft gluons should be largely unscreened because the condensate is a color singlet and colored excitations are gapped. These unscreened gluon propagators are supported by lattice simulations for two-color QCD [11,77–81].

With soft gluons being unscreened, the size of the gap is $\sim\Lambda_{\rm QCD}$ or can be even larger. To see this, we parametrize the soft gluon exchange forces as

$$D_g(q) = \Theta(\Lambda - |\vec{q}|)\,\frac{c}{\Lambda^2}\,, \qquad c \sim g_s^2 \sim 4\pi\alpha_s(\Lambda) \sim O(10)\,, \tag{1}$$

where c/Λ^2 is the typical strength for a soft momentum transfer $|\vec{q}| < \Lambda$. This model has been used for quarkyonic chiral spirals [82–84] and QCD in a magnetic field [85–87] to yield the gap equation local in momentum space (Figure 3). The resultant gap is $\sim\Lambda$, and we expect the same happens for the soft gluonic part in isospin QCD.

Now, the gap equation reads

$$\Delta \sim \frac{c}{\Lambda^2}\int_{\vec{l}}\Theta(\Lambda^2 - |\vec{l}-\vec{p}|^2)\,\frac{\Delta}{\sqrt{\left(E(\vec{l})-\mu_I\right)^2+\Delta^2}}\,. \tag{2}$$

Decomposing the loop momentum as $\vec{l} = (|\vec{p}| + \delta l_\parallel)\mathbf{e}_p + \vec{l}_\perp$ with $|\vec{p}| \simeq \mu_I$, the conservative estimate for the range is $|\delta l_\parallel| \lesssim \Lambda$ and $|\vec{l}_\perp| \lesssim \Lambda$. Then, one can simplify the gap equation into (v_F: Fermi velocity)

$$1 \sim \frac{c}{(2\pi)^3\Lambda^2}\int_{-\Lambda}^{\Lambda} \mathrm{d}\delta l_\parallel \int_{|\vec{l}_\perp|\lesssim\Lambda} \mathrm{d}\vec{l}_\perp \frac{1}{\sqrt{\left(v_f\delta l_\parallel + \frac{\vec{l}_\perp^2}{2\mu_I}\right)^2 + \Delta^2}}\,. \tag{3}$$

If $\Lambda \ll \mu_I$ and $\vec{l}_\perp^2/2\mu_I \lesssim \Lambda^2/2\mu_I \ll \Delta$ hold, we can omit the $\vec{l}_\perp^2/\mu_I$ term in the range of integral to factorize the $\vec{l}_\perp$ integral. The condition $\Lambda^2/2\mu_I \ll \Delta$ will be checked a posteriori. At this stage, the equation loses the μ_I-dependence and so does the solution. Further calculation reads

$$1 \sim \frac{c}{4\pi^2}\int_0^{\Lambda} \mathrm{d}\delta l_\parallel \frac{1}{\sqrt{(v_f\delta l_\parallel)^2 + \Delta^2}} \sim \frac{c}{4\pi^2}\ln\frac{\Lambda}{\Delta}\,. \tag{4}$$

Thus, the gap is $\Delta \sim \Lambda \mathrm{e}^{-4\pi^2/c} \sim \Lambda \mathrm{e}^{-\pi/\alpha_s(\Lambda)}$. For a stronger coupling, the gap Δ grows to Λ, and the condition $\Lambda^2/2\mu_I \ll \Delta$ is satisfied.

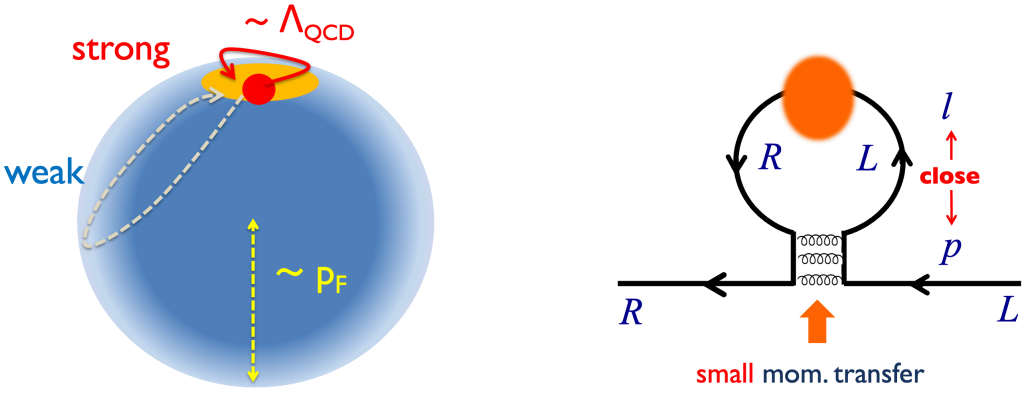

Figure 3. The gap created by soft gluons. The self-energies caused by soft gluons are not very sensitive to the size of the Fermi surface because quarks fluctuate only within small domain. The produced gap is characterized by soft gluons and is supposed to be $\sim\Lambda_{\mathrm{QCD}}$, until hard gluon processes dominate over soft gluon processes.

The present arguments show that, even at large μ or large quark Fermi momenta, non-perturbative phenomena characterized by Λ_{QCD} are still possible. This continues until screening effects set in. When μ_I is sufficiently large, we should also add hard gluon contributions, which can be treated within the weak coupling method; this hard contributions are sensitive to the phase space around the Fermi surface and hence to μ_I. As we see later, the gap (which is insensitive to μ_I) adds the *power corrections*, $\sim+\mu_I^2\Delta^2 \sim \mu_I^2\Lambda_{\mathrm{QCD}}^2$, to the pressure $P(\mu_I)$. These power corrections, not capable within perturbative computations, have played important roles in QCD phenomenology [88–90] and also seem essential to describe the lattice simulation data at large density [50,51].

3. A Quark–Meson Model: Mean Field Treatments

Now, we consider a practical description of a three-flavor quark–meson model. The Lagrangian is

$$\mathcal{L} = \mathcal{L}_{\mathrm{Y}} + \mathcal{L}_{\mathrm{kin}}^{M} - V_{\mathrm{sym}} - V_{\mathrm{SB}} - V_{\mathrm{anom}}\,. \tag{5}$$

The quark with the Yukawa interaction takes the form

$$\begin{aligned}\mathcal{L}_{\mathrm{Y}} &= \bar{q}\left[\mathrm{i}\partial\!\!\!/ + \mu_I\tau_3\gamma_0 - g(\sigma_a + \mathrm{i}\gamma_5\pi_a)\lambda_a\right]q \\ &= \bar{q}\left[\mathrm{i}\partial\!\!\!/ + \mu_I\tau_3\gamma_0\right]q - g\phi_a\left[\bar{q}_L\lambda_a q_R\right] - g\phi_a^*\left[\bar{q}_R\lambda_a q_L\right],\end{aligned} \tag{6}$$

where $\phi_a = \sigma_a + \mathrm{i}\pi_a$. We have scalar and pseudoscalar flavor nonets. In our notation, the isospin chemical potential is $\mu_I = \mu_u = -\mu_d$, coupled to $\bar{q}\gamma_0\tau_3 q$ rather than the isospin density operator $\bar{q}\gamma_0\frac{\tau_3}{2}q$ in the conventional sense.

The mesonic Lagrangian with the isospin chemical potential is

$$\begin{aligned}\mathcal{L}^M_{\rm kin} = &\sum_{a=0,3,8}\frac{1}{2}|\partial_\mu\phi_a|^2 \\ &+ (\partial_\mu + 2\mathrm{i}\mu_I\delta^0_\mu)a_0^+(\partial^\mu - 2\mathrm{i}\mu_I\delta^\mu_0)a_0^- + (\partial_\mu + 2\mathrm{i}\mu_I\delta^0_\mu)\pi^+(\partial^\mu - 2\mathrm{i}\mu_I\delta^\mu_0)\pi^- \\ &+ (\partial_\mu + \mathrm{i}\mu_I\delta^0_\mu)\kappa^+(\partial^\mu - \mathrm{i}\mu_I\delta^\mu_0)\kappa^- + (\partial_\mu + \mathrm{i}\mu_I\delta^0_\mu)K^+(\partial^\mu - \mathrm{i}\mu_I\delta^\mu_0)K^- \\ &+ (\partial_\mu + \mathrm{i}\mu_I\delta^0_\mu)\bar{\kappa}^0(\partial^\mu - \mathrm{i}\mu_I\delta^\mu_0)\kappa^0 + (\partial_\mu + \mathrm{i}\mu_I\delta^0_\mu)\bar{K}^0(\partial^\mu - \mathrm{i}\mu_I\delta^\mu_0)K^0\,,\end{aligned} \tag{7}$$

where isotriplet $(\sigma_{a=1-3}, \pi_{a=1-3}) = (a_0, \pi)$ and two isodoublets $(\sigma_{a=4-7}, \pi_{a=4-7}) = (\kappa, K)$ couple to the isospin chemical potential. The field normalization for isospin-charged fields are $a_0^\pm = (\sigma_1 \pm \mathrm{i}\sigma_2)/\sqrt{2}$, and so on. Since τ_3 commutes with the isospin rotation operator around the I_3-axis, the $\mathrm{U}(1)_{I_3}$ symmetry is preserved at the level of the Lagrangian. This symmetry is broken when pions condense.

The mesonic potential consists of three pieces

$$V_M(\phi, \phi^*) = V_{\rm sym} + V_{\rm SB} + V_{\rm anom}\,, \tag{8}$$

with a U(3) symmetric potential

$$V_{\rm sym} = -\frac{m_M^2}{4}\mathrm{tr}\left[\mathcal{M}\mathcal{M}^\dagger\right] + \frac{\lambda}{48}\mathrm{tr}\left[\left(\mathcal{M}\mathcal{M}^\dagger\right)^2\right], \qquad \mathcal{M} = \phi_a\lambda_a\,, \tag{9}$$

and a symmetry-breaking term associating the current quark masses,

$$V_{\rm SB} = -\frac{c}{2}\mathrm{tr}\left[\hat{m}_q^\dagger\mathcal{M} + \hat{m}_q\mathcal{M}^\dagger\right], \qquad \hat{m}_q = \mathrm{diag.}(m_l, m_l, m_s)\,, \tag{10}$$

and the Kobayashi–Maskawa–'t Hooft (KMT) interaction

$$V_{\rm anom} = -\frac{K}{2}\left[\det\mathcal{M} + \det\mathcal{M}^\dagger\right]. \tag{11}$$

which is responsible for the $\mathrm{U}_A(1)$ breaking.

Increasing μ_I, the excitation energies of mesons including u or $\bar{d}$ are reduced, i.e., the excitation energies of $\sigma^+, \pi^+, a_0^+, K^+, \cdots$ decrease linearly as a function of μ_I. As we see shortly, the tree level analyses show that the lightest pion condenses first, and then the reduction in energies for the other mesons is stopped; no other mesons condense. At the tree level, this is interpreted as the effective repulsion between condensed pions and the other mesons. We assume this holds even after including loop corrections. Thus, we take the mean field as

$$\mathcal{M}_{\rm MF} = \begin{bmatrix} \langle\sigma\rangle & \mathrm{i}\langle\pi_1\rangle & 0 \\ \mathrm{i}\langle\pi_1\rangle & \langle\sigma\rangle & 0 \\ 0 & 0 & \langle\sigma_s\rangle \end{bmatrix}, \quad \sigma = \sqrt{\frac{2}{3}}\sigma_0 + \sqrt{\frac{1}{3}}\sigma_8\,, \quad \sigma_s = \sqrt{\frac{2}{3}}\sigma_0 - 2\sqrt{\frac{1}{3}}\sigma_8\,. \tag{12}$$

Here, we could choose π_1 fields for condensed fields without loss of generality since the Lagrangian has the $\mathrm{U}(1)_{I_3}$ symmetry. The mean-field Yukawa term now takes the form $(q_l = u, d)$

$$\mathcal{L}^{\rm MF}_{\rm Y} = \bar{q}_l\left[\mathrm{i}\partial\!\!\!/ + \mu_I\tau_3\gamma_0 - M_l - \mathrm{i}\gamma_5\lambda_1\Delta\right]q_l + \bar{s}\left[\mathrm{i}\partial\!\!\!/ - M_s\right]s\,, \tag{13}$$

where we write $M_l = g\langle\sigma_l\rangle$, $M_s = g\langle\sigma_s\rangle$, and $\Delta = g\langle\pi_1\rangle$. Substituting the mean fields into the potentials, one finds

$$V_{\rm sym}^{\rm MF} = -\frac{m_M^2}{2g^2}(M_l^2+\Delta^2) + \frac{\lambda}{24g^4}\left(M_l^2+\Delta^2\right)^2 - \frac{m_M^2}{4g^2}M_s^2 + \frac{\lambda}{48g^4}M_s^4 \tag{14}$$

and ($h_l = 2cm_l, h_s = 2cm_s$)

$$V_{\rm SB}^{\rm MF} = -\frac{h_l}{g}M_l - \frac{h_s}{2g}M_s\,, \qquad V_{\rm anom}^{\rm MF} = -\frac{K}{g^3}\left(M_l^2+\Delta^2\right)M_s\,. \tag{15}$$

Below, we first examine the effective potential at the tree level which includes only the mesonic degrees of freedom. The quark dynamics manifestly enters only after including the quark loops. As we see later, the quark loops change the structure of theories and impose important constraints on the meson mean fields.

4. Purely Hadronic Descriptions: Tree Level Analyses

4.1. Gap Equations at Tree Level

We first study the tree level potential, including only meson degrees of freedom. Combining the potentials with the terms, including the chemical potential in $\mathcal{L}_{\rm kin}^M$, the effective potential at the tree level is

$$\Omega_0 = -\frac{2\mu_I^2}{g^2}\Delta^2 + V_{\rm sym}^{\rm MF} + V_{\rm SB}^{\rm MF} + V_{\rm anom}^{\rm MF}\,. \tag{16}$$

The gap equations are

$$\begin{aligned}
\frac{\partial\Omega_0}{\partial M_l} &= \frac{M_l}{g^2}\left[-m_M^2 + \frac{\lambda}{6g^2}\left(M_l^2+\Delta^2\right) - \frac{2K}{g}M_s - \frac{gh_l}{M_l}\right] = 0\,,\\
\frac{\partial\Omega_0}{\partial M_s} &= \frac{M_s}{2g^2}\left[-m_M^2 + \frac{\lambda}{6g^2}M_s^2 - \frac{2K}{g}\frac{M_l^2}{M_s} - \frac{gh_s}{M_s}\right] = 0\,,\\
\frac{\partial\Omega_0}{\partial\Delta} &= \frac{\Delta}{g^2}\left[-4\mu_I^2 - m_M^2 + \frac{\lambda}{6g^2}\left(M_l^2+\Delta^2\right) - \frac{2K}{g}M_s\right] = 0\,.
\end{aligned} \tag{17}$$

We can show that $gh_l/M_l^{\rm vac} = (m_\pi^{\rm vac})^2$. We combine the first and third equations to derive a simple relation,

$$\frac{\partial\Omega_0}{\partial\Delta} = \frac{\Delta}{g^2}\left[-4\mu_I^2 + \frac{gh_l}{M_l}\right] = 0\,, \qquad \frac{\partial^2\Omega_0}{(\partial\Delta)^2} = \frac{1}{g^2}\left[-4\mu_I^2 + \frac{gh_l}{M_l} + \frac{\lambda}{3g^2}\Delta^2\right]. \tag{18}$$

The curvature with respect to Δ is positive for small μ_I so that $\Delta = 0$ is favored. Then, the gap equation is the same as in the vacuum case; in this domain $M_l = M_l^{\rm vac}$ and $gh_l/M_l^{\rm vac} = (m_\pi^{\rm vac})^2$ holds. The curvature becomes negative for $m_\pi^{\rm vac} \geq 2\mu_I$, leading to the scaling $M_l \sim 1/\mu_I^2$. This in turn leads to $\Delta^2 \sim 1/M_l \sim \mu_I^2$ from the condition $\partial\Omega_0/\partial M_l = 0$. The strange quark is affected by the isospin density only through the anomaly term.

4.2. Meson Kinetic and Mass Matrices at Tree Level

We now quickly review the properties of mesons in a medium of condensed pions. We first take a look at the excitation energies of charged mesons in the low-density domain. Then, the Lagrangian has the following structure ($E = \sqrt{\vec{p}^2+m^2}$):

$$\frac{1}{2}[\phi_+,\phi_-]\begin{bmatrix} 0 & (p_0+N_I\mu_I)^2 - E^2 \\ (p_0+N_I\mu_I)^2 - E^2 & 0 \end{bmatrix}\begin{bmatrix}\phi_+\\ \phi_-\end{bmatrix}, \tag{19}$$

where $N_I = 2$ for the isotriplet and $N_I = 1$ for the isodoublet. The spectra are found to be

$$\omega_\pm(\vec{p}) = E(\vec{p}) \pm N_I \mu_I \,. \qquad \text{(in normal phase)} \tag{20}$$

Mesons with positive isospins have energy reduction. This continues until one of those mesons condenses. The pions are the lightest and have the largest isospin $N_I = 2$, so they condense first, at $\mu_I = m_\pi^{\rm vac}/2$.

Before the pion condensation, a pair of positive- and negative-charged mesons maintains the μ_I-independence of the thermodynamics. The thermodynamic potential from a (non-interacting) meson for $N_I\mu_I \le E(\vec{p}=0)$ is

$$\Omega = \frac{1}{2}\int_{\vec{p}} \left(|E + N_I\mu_I| + |E - N_I\mu_I|\right) \;\to\; \frac{1}{2}\int_{\vec{p}} \left(E + N_I\mu_I + E - N_I\mu_I\right) = \int_{\vec{p}} E\,, \tag{21}$$

after the μ_I terms cancel. The resulting energy is the same zero point energy as in the vacuum. The expression is valid until $N_I\mu_I$ reaches the meson mass.

After the pions condense, mesons with an energy reduction in the normal phase are now subject to effective repulsions, and hence the gap remains in the excitation energies. In addition, condensed pions supply isospin and parity violating sources so that various mesons mix. At the tree level, the mixing is caused through the quartic and the KMT interaction. We read off the meson mass matrices masses by looking at the quadratic order of the potential

$$\begin{aligned} V_M^{\rm quad} &= \frac{\partial^2 \tilde{V}_0}{\partial\phi_a \partial\phi_b^*}\phi_a\phi_b^* + \frac{1}{2}\frac{\partial^2 \tilde{V}_0}{\partial\phi_a\partial\phi_b}\phi_a\phi_b + \frac{1}{2}\frac{\partial^2 \tilde{V}_0}{\partial\phi_a^*\partial\phi_b^*}\phi_a^*\phi_b^* + \cdots \\ &= \frac{\partial^2 \tilde{V}_0}{\partial\phi_a \partial\phi_b^*}\left[\sigma_a\sigma_b + \pi_a\pi_b\right] + {\rm Re}\frac{\partial^2 \tilde{V}_0}{\partial\phi_a\partial\phi_b}\left(\sigma_a\sigma_b - \pi_a\pi_b\right) - {\rm Im}\frac{\partial^2 \tilde{V}_0}{\partial\phi_a\partial\phi_b}\left(\sigma_a\pi_b + \pi_a\sigma_b\right) \end{aligned} \tag{22}$$

where we evaluate the second derivative at the mean field values, and also use the fact that $\frac{\partial^2 \tilde{V}_0}{\partial\phi_a\partial\phi_b^*}\big|_{\rm MF}$ is real. The mass matrices for σ and π are

$$m^2_{\sigma_a\sigma_b} = 2\left[\frac{\partial^2 \tilde{V}_0}{\partial\phi_a\partial\phi_b^*} + {\rm Re}\frac{\partial^2 \tilde{V}_0}{\partial\phi_a\partial\phi_b}\right], \quad m^2_{\pi_a\pi_b} = 2\left[\frac{\partial^2 \tilde{V}_0}{\partial\phi_a\partial\phi_b^*} - {\rm Re}\frac{\partial^2 \tilde{V}_0}{\partial\phi_a\partial\phi_b}\right], \tag{23}$$

and the parity-breaking σ–π couplings induced by the pion condensate are

$$m^2_{\sigma_a\pi_b} = -2{\rm Im}\frac{\partial^2 \tilde{V}_0}{\partial\phi_a\partial\phi_b} \quad (\propto \Delta)\,. \tag{24}$$

The pion condensate $\pi_1 \sim u\bar{d} + d\bar{u}$ induces the conversion $u \leftrightarrow d$ and $\bar{u} \leftrightarrow \bar{d}$, and also causes the conversion between the σ and π sectors. For light flavors, all channels but $\pi_3, \sigma_3 \sim u\bar{u} - d\bar{d}$ mix. The exceptional π_3 and σ_3 are protected from the mixing because of the G-parity [91] type symmetries as we discuss shortly. All kaons are mixed with one another. But the isodoublets do not mix with the isoscalar nor the isovector since the condensed π_1 supply integer isospins.

To understand the decoupling of π_3 and σ_3 from the others, we consider the unitary transformations induced by

$$P_{I_3}(\theta) = P{\rm e}^{{\rm i}\theta I_3}\,, \qquad C_{I_1}(\theta) = C{\rm e}^{{\rm i}\theta I_1}\,, \tag{25}$$

where P and C are parity and charge conjugation, respectively. We define $C^{-1}\pi_+ C = \pi_-$ and $C^{-1}\pi_3 C = \pi_3$ so that the G-parity is -1 for all pions. In this definition, $C^{-1}\pi_1 C = \pi_1$ and $C^{-1}\pi_2 C = -\pi_2$.

The P_{I_3} symmetry holds in our U_{I_3} symmetric Lagrangian for any θ. The question is whether this symmetry is spontaneously broken or not. The π_1 condensate under this symmetry transforms to

$$P_{I_3}^{-1}(\theta)\pi_1 P_{I_3}(\theta) \sim P^{-1}\left(e^{-i\theta}\bar{u}i\gamma_5 d + e^{i\theta}\bar{d}i\gamma_5 u\right)P = -\left(e^{-i\theta}\bar{u}i\gamma_5 d + e^{i\theta}\bar{d}i\gamma_5 u\right), \tag{26}$$

which in general is the mixture of π_1 and π_2. But setting $\theta = \pi$ and writing $\mathcal{P}_{I_3} \equiv P_{I_3}(\pi)$, we conclude that $\mathcal{P}_{I_3}^{-1}\pi_1\mathcal{P}_{I_3} = \pi_1$. Thus, the $\mathcal{P}_{I_3}$ parity is conserved in the presence of the π_1 condensates. We also note that $\mathcal{P}_{I_3}$ parity is also not violated by σ and σ_s condensates. Thus, $\mathcal{P}_{I_3}$ can be used to classify various mesons. Under the $\mathcal{P}_{I_3}$ transformation, the isoscalar and isovectors transform as

$$\mathcal{P}_{I_3}^{-1}(\sigma_{0,3,8}, \pi_{1,2})\mathcal{P}_{I_3} = +(\sigma_{0,3,8}, \pi_{1,2}), \quad \mathcal{P}_{I_3}^{-1}(\sigma_{1,2}, \pi_{0,3,8})\mathcal{P}_{I_3} = -(\sigma_{1,2}, \pi_{0,3,8}). \tag{27}$$

Next, we consider $C_{I_1}(\theta)$. First, we note that the isospin density is invariant for $\mathcal{C}_{I_1} \equiv C_{I_1}(\pi)$,

$$C_{I_1}^{-1}(\theta)\left(\bar{u}u - \bar{d}d\right)C_{I_1}(\theta) = -C^{-1}\left(\bar{u}u - \bar{d}d\right)C = \bar{u}u - \bar{d}d, \tag{28}$$

where we used $e^{-i\pi I_1}(u, d)e^{i\pi I_1} = (d, u)$. The Lagrangian is also invariant. The condensates π_1, σ, and σ_s are also invariant. Under the $\mathcal{C}_{I_1}$ transformation, the isoscalar and isovectors transform as

$$\mathcal{C}_{I_1}^{-1}\phi_{0,1,2,8}\mathcal{C}_{I_1} = +\phi_{0,1,2,8}, \quad \mathcal{C}_{I_1}^{-1}\phi_3\mathcal{C}_{I_3} = -\phi_3. \tag{29}$$

Combining these symmetries, the isoscalar and isovector sectors can be decomposed into

$$\sigma_3, \quad \pi_3, \quad (\sigma_0, \sigma_8; \pi_1, \pi_2), \quad (\pi_0, \pi_8; \sigma_1, \sigma_2). \tag{30}$$

Meanwhile, for the isodoublet sectors,

$$\left(\sigma_4, \sigma_5, \sigma_6, \sigma_7; \pi_4, \pi_5, \pi_6, \pi_7\right) \tag{31}$$

are all mixed.

4.2.1. The Spectra of σ_3, π_3, and $(\sigma_0, \sigma_8; \pi_1, \pi_2)$

Here, we display some analytic expressions for σ_3, π_3, and $(\sigma_0, \sigma_8; \pi_1, \pi_2)$. The σ_3 and π_3 decouple from the other modes, and the mass matrices are

$$\begin{aligned} m_{\pi_3}^2 &= -m_M^2 + \frac{\lambda}{6g^2}(M_l^2 + \Delta^2) - \frac{2K}{g}M_s = 4\mu_I^2, \\ m_{\sigma_3}^2 &= -m_M^2 + \frac{\lambda}{2g^2}(M_l^2 + \Delta^2) + \frac{2K}{g}M_s = 4\mu_I^2 + \frac{\lambda}{3g^2}(M_l^2 + \Delta^2) + \frac{4K}{g}M_s, \end{aligned} \tag{32}$$

where for π_3, we use the gap equation. For these neutral modes, the excitation energies directly coincide with the mass $\omega_{\pi_3,\sigma_3} = m_{\pi_3,\sigma_3}$.

Next, we look into the charged sector. The pion mass matrices are

$$\begin{aligned} m_{\pi_1}^2 &= -m_M^2 + \frac{\lambda}{6g^2}(M_l^2 + 3\Delta^2) - \frac{2K}{g}M_s = 4\mu_I^2 + \frac{\lambda}{3g^2}\Delta^2, \\ m_{\pi_2}^2 &= -m_M^2 + \frac{\lambda}{6g^2}(M_l^2 + \Delta^2) - \frac{2K}{g}M_s = 4\mu_I^2, \end{aligned} \tag{33}$$

and the neutral σ sector has the mass matrices

$$m_{\sigma_0}^2 = -m_M^2 + \frac{\lambda}{18g^2}\left[6M_l^2 + 3M_s^2 + 2\Delta^2\right] - \frac{4K}{3g}\left[2M_l + M_s\right],$$
$$m_{\sigma_8}^2 = -m_M^2 + \frac{\lambda}{18g^2}\left[3M_l^2 + 6M_s^2 + 2\Delta^2\right] + \frac{2K}{3g}\left[4M_l - M_s\right]. \tag{34}$$

The mixing is induced by

$$m_{\sigma_0\pi_1}^2 = \frac{\sqrt{2}K}{\sqrt{3}g}\Delta, \qquad m_{\sigma_0\sigma_8}^2 = \frac{\lambda\sqrt{2}}{12g^2}\Delta^2 - \frac{\lambda\sqrt{2}}{36g^2}\delta M_s^2 + \frac{\sqrt{2}K}{3g}\delta M_s. \tag{35}$$

The coupling between the $\sigma_{0,8}$ and $\pi_{1,2}$ sectors is induced through the convolution of the $\mathrm{U}_A(1)$ anomaly and the pion condensate. Meanwhile, the mixing between σ_0 and σ_8 is due to the explicit SU(3) breaking, which appears through $\delta M_s = M_s - M_l$ and the meson condensates existing only in the u, d sector.

The isospin chemical potentials in the kinetic terms and mass terms together yield the massless modes. For a simple illustration, we consider the case where K is small. In this approximation, $\pi_{1,2}$ and $\sigma_{0,8}$ decouple. Now, the quadratic terms in $\pi_{1,2}$ are

$$\begin{bmatrix} p_0^2 - m_{\pi_1}^2 + 4\mu_I^2 & 4\mathrm{i}\mu_I p_0 \\ -4\mathrm{i}\mu_I p_0 & p_0^2 - m_{\pi_2}^2 + 4\mu_I^2 \end{bmatrix} = \begin{bmatrix} p_0^2 - \frac{\lambda}{3g^2}\Delta^2 & 4\mathrm{i}\mu_I p_0 \\ -4\mathrm{i}\mu_I p_0 & p_0^2 \end{bmatrix}. \tag{36}$$

We use the expression of $m_{\pi_1}^2$ and $m_{\pi_2}^2$. The determinant of the matrix becomes zero at $p_0 = 0$, reflecting that there is a massless mode associated with the spontaneous breakdown of the U_{I_3} symmetry.

4.2.2. The Spectra of $(\sigma_{4-7}; \pi_{4-7})$

Next, we discuss the isodoublet (kaon) sector. The diagonal part is

$$\begin{aligned} m_{\pi_{4-7}}^2 &= -m_M^2 + \frac{\lambda}{6g^2}(M_l^2 + M_s^2 - M_l M_s + \Delta^2) - \frac{2K}{g}M_l \\ &= 4\mu_I^2 + \frac{\lambda}{6g^2}M_l(M_s - M_l) + \frac{2K}{g}(M_s - M_l), \\ m_{\sigma_{4-7}}^2 &= -m_M^2 + \frac{\lambda}{6g^2}(M_l^2 + M_s^2 + M_l M_s + \Delta^2) + \frac{2K}{g}M_l \\ &= 4\mu_I^2 + \frac{\lambda}{6g^2}M_s(M_s + M_l) + \frac{2K}{g}(M_s + M_l), \end{aligned} \tag{37}$$

where we use the gap equation for the pion sector. The difference in the mass matrices between the pion and kaon sectors comes from the effective quark mass. The mixing matrices are

$$\begin{aligned} m_{\sigma_4,\sigma_7}^2 &= -m_{\sigma_5,\sigma_6}^2 = -m_{\pi_4,\pi_7}^2 = m_{\pi_5,\pi_6}^2 = \frac{\lambda}{24g^2}\Delta\delta M_s, \\ m_{\sigma_4\pi_6}^2 &= m_{\sigma_5\pi_7}^2 = m_{\pi_4\sigma_6}^2 = m_{\pi_5\sigma_7}^2 = \frac{\lambda}{24g^2}\Delta\big(M_l + M_s\big) - \frac{K}{g}\Delta. \end{aligned} \tag{38}$$

These form a 8×8 matrix and need numerical analyses for the determination of the spectra.

To obtain analytic insights, we consider the case where $M_l, M_s \ll \mu_I$ for which the mixing is neglected compared to the diagonal part. Combining the mass matrices with the kinetic term, (we write $m_K^2 = m_{4-7}^2$)

$$\begin{bmatrix} p_0^2 - m_K^2 + \mu_I^2 & 2\mathrm{i}\mu_I p_0 \\ -2\mathrm{i}\mu_I p_0 & p_0^2 - m_K^2 + \mu_I^2 \end{bmatrix} \sim \begin{bmatrix} p_0^2 - 3\mu_I^2 & 2\mathrm{i}\mu_I p_0 \\ -2\mathrm{i}\mu_I p_0 & p_0^2 - 3\mu_I^2 \end{bmatrix}. \tag{39}$$

For kaons being the isodoublet, the energy reduction associated with the chemical potential is weaker than in the pion, and hence the μ_I terms do not cancel. The excitation energies manifestly depend on μ_I,

$$\omega_K \sim \mu_I, \ 3\mu_I . \tag{40}$$

The same also holds for the scalar meson κ.

5. Quark Descriptions

Now, we include loops made of mean-field quark propagators. We keep only one loop with the leading N_c contributions; quark loops for the vertex corrections are neglected. In the counting of loops, the quark contributions appear as radiative "corrections" to the tree level, but in fact the quark contributions should be regarded as leading-order contributions at finite density [50]; indeed, as μ_I increases, the quark contributions dominate over hadronic contributions and change the structure of gap equations and EOS.

5.1. The Structure of the Effective Potential

Beyond tree calculations, the parameters in the effective potential must be also reinterpreted as bare parameters which are split into the renormalized parameters and counter terms. First, we attach an index B to fields ϕ, q, m_M, and so on, and factor out the renormalized parameters and fields [50],

$$\begin{aligned}
\phi_B &= Z_\phi^{1/2}\phi, \quad q_B = Z_q^{1/2} q, \\
g_B &= \tilde{Z}_g Z_q^{-1} Z_\phi^{-1/2} g = Z_g g, \\
(m_M^2)_B &= \tilde{Z}_{m^2} Z_\phi^{-1} m_M^2 = Z_{m^2} m_M^2, \\
\lambda_B &= \tilde{Z}_\lambda Z_\phi^{-2}\lambda = Z_\lambda \lambda, \\
(h_l)_B &= \tilde{Z}_{h_l} Z_\phi^{-1/2} h = Z_{h_l} h_l, \\
(h_s)_B &= \tilde{Z}_{h_s} Z_\phi^{-1/2} h = Z_{h_s} h_s .
\end{aligned} \tag{41}$$

We also use $\delta Z_i = Z_i - 1$ with $i = \phi, q, g$, and so on. The $\tilde{Z}_i$ represents the radiative corrections without those for the external lines. The loop corrections to the quark self-energies and quark–meson vertices appear only through meson loops and hence

$$Z_\psi = 1 + O(1/N_c), \quad \tilde{Z}_g = 1 + O(1/N_c) . \tag{42}$$

Meanwhile, the meson self-energies and tadpole contain quark loops of $O(N_c)$ which are combined with $g^2 \sim 1/N_c$ vertices to yield

$$\begin{aligned}
&Z_\phi = 1 + O(g^2 N_c), \quad \tilde{Z}_{m^2} = 1 + O(g^2 N_c), \\
&\tilde{Z}_h = 1 + O(g^2 N_c), \quad \tilde{Z}_\lambda = 1 + O(g^4 N_c/\lambda) .
\end{aligned} \tag{43}$$

and hence one must keep these corrections. It is useful to note that the relation

$$g_B \phi_B = g\phi, \quad Z_g = Z_\phi^{-1/2}, \tag{44}$$

in the large N_c limit. With the first relation, the dynamically generated quark mass and gap are RG invariant. The second relation tells that the running of g^2 can be studied by examining the meson propagators.

The effective potential up to one-loop consists of three type of terms

$$\Omega = \Omega_0 + \Omega_{\text{c.t.}} + \Omega_q . \tag{45}$$

The Ω_0 takes the same form as in the tree level, but the parameters are to be interpreted as renormalized ones. The $\Omega_{\rm c.t.}$ includes the counter terms originating from the splitting, e.g., $\lambda_B = \lambda + \delta\lambda$,

$$\begin{aligned}\Omega_{\rm c.t.} \;&= -\delta Z_\phi \frac{2\mu_I^2}{g^2}\Delta^2 - \frac{\delta m_M^2}{2g^2}(M_l^2+\Delta^2) + \frac{\delta\lambda}{24g^4}\left(M_l^2+\Delta^2\right)^2 - \frac{\delta h_l}{g}M_l \\ &\quad - \frac{\delta m_M^2}{4g^2}M_s^2 + \frac{\delta\lambda}{48g^4}M_s^4 - \frac{\delta h_s}{2g}M_s - \frac{\delta K}{g^3}\left(M_l^2+\Delta^2\right)M_s\,. \end{aligned} \tag{46}$$

The quark contribution is

$$\Omega_q = -2N_{\rm c}\int_{\vec p}\left(\xi_+ + \xi_- + E_s\right), \tag{47}$$

where $E_l = \sqrt{\vec p^2 + M_l^2}$ and $E_s = \sqrt{\vec p^2 + M_s^2}$, and

$$\xi_- = \xi_u = \xi_{\bar d} = \sqrt{\left(E_l - \mu_I\right)^2 + \Delta^2}\,, \qquad \xi_+ = \xi_d = \xi_{\bar u} = \sqrt{\left(E_l + \mu_I\right)^2 + \Delta^2}\,. \tag{48}$$

In the u,d-quark sector, quarks have the energy dispersion of the BCS type.

For small $\mu_I \le m_\pi/2 \le M_l$, the pion condensate is absent. Then, the chemical potential disappears from the Ω_q,

$$\sqrt{\left(E_l + \mu_I\right)^2 + \Delta^2} + \sqrt{\left(E_l - \mu_I\right)^2 + \Delta^2} \;\to\; (E_l + \mu_I) + (E_l - \mu_I) = 2E_l\,, \tag{49}$$

reflecting the Sliver Blaze property that the isospin density n_I begins to change only when either $\mu_I \ge M_l$ or $\Delta \ne 0$ are satisfied. In the present case, $\Delta \ne 0$ is the driving force.

The Ω_q is UV divergent. This divergence is canceled by the counter terms from the masses, couplings, and field normalization factor from the mesonic Lagrangian. We isolate the divergences as [92]

$$\Omega_q = \Omega_l^{\rm R} - 2N_{\rm c}\int_{\vec p}\left[2\sqrt{E_q^2+\Delta^2} + \frac{\mu_I^2\Delta^2}{(E_q^2+\Delta^2)^{3/2}} + E_s\right] \tag{50}$$

where the twice-subtracted energy density, including only u,d-quark contributions, is

$$\Omega_l^{\rm R} = -2N_{\rm c}\int_p\left[\xi_+ + \xi_- - 2\sqrt{E_q^2+\Delta^2} - \frac{\mu_I^2\Delta^2}{(E_q^2+\Delta^2)^{3/2}}\right]. \tag{51}$$

The Ω_l^R is UV finite and vanishing when $\mu_I = 0$ and $\Delta = 0$. At a large density, the subtracted energy scales as $\Omega_l^R \simeq \mu_I^4$, dominating the thermodynamic potential.

To understand the physical meaning of the subtracted potential Ω_l^R at large μ_I, it is instructive to consider the $\Delta \to 0$ limit and decompose the integral into the $E_l \le \mu_I$ and $E_l \ge \mu_I$ domains. For $E_l \le \mu_I$,

$$\int_{\vec p}\Theta(\mu_I - E_l)\left(\,|E_l+\mu_I| + |E_l-\mu_I| - 2E_l\,\right) = 2\int_{\vec p}\Theta(\mu_I - E_l)\left(\mu_I - E_l\right), \tag{52}$$

and for $E_I \ge \mu_l$,

$$\int_{\vec p}\Theta(E_l - \mu_I)\left(\,|E_l+\mu_I| + |E_l-\mu_I| - 2E_l\,\right) = 0\,. \tag{53}$$

Thus, Ω_l^R at $\Delta = 0$ is nothing but the standard quasi-particle contributions to the thermodynamic potential.

The divergent piece in Ω_q is evaluated in the $\overline{MS}$ scheme,

$$\Omega_q^{\rm UV} = \frac{2N_{\rm c}}{(4\pi)^2}(M_l^2+\Delta^2)^2\left[\frac{1}{\epsilon}+\frac{3}{2}+\ln\frac{\Lambda^2}{M_l^2+\Delta^2}\right] - \frac{8N_{\rm c}}{(4\pi)^2}\mu_I^2\Delta^2\left[\frac{1}{\epsilon}+\ln\frac{\Lambda^2}{M_l^2+\Delta^2}\right] + \frac{N_{\rm c}}{(4\pi)^2}M_s^4\left[\frac{1}{\epsilon}+\frac{3}{2}+\ln\frac{\Lambda^2}{M_s^2}\right], \tag{54}$$

where Λ is the renormalization scale. In the $\overline{MS}$ scheme, the counter terms are used to absorb only the $1/\epsilon$ terms. Then, the counter terms are fixed as

$$\delta m_M^2 = 0\,, \quad \delta h_{l,s} = 0\,, \quad \delta\lambda = -\frac{48N_{\rm c}g^4}{(4\pi)^2\epsilon}\,, \quad \delta Z_\phi = -\frac{4N_{\rm c}g^2}{(4\pi)^2\epsilon}\,, \quad \delta K = 0\,. \tag{55}$$

In our previous studies, we further discussed the on-mass-shell renormalization to tune the pole positions of π and σ. We do this when we fix parameters of our model.

Putting everything together, the effective potential $\Omega = \Omega_0 + \Omega_{\rm c.t.} + \Omega_q$ is reorganized as

$$\Omega = \Omega_l + \Omega_s + \Omega_{\rm mix} \tag{56}$$

where the contributions from u,d-quarks are

$$\Omega_l = \Omega_l^R - \frac{m_M^2}{2g^2}(M_l^2+\Delta^2) + \frac{\lambda}{24g^4}\left(M_l^2+\Delta^2\right)^2 - \frac{h_l}{g}M_l + \frac{2N_{\rm c}}{(4\pi)^2}(M_l^2+\Delta^2)^2\left[\frac{3}{2}-\ln\frac{M_l^2+\Delta^2}{M_0^2}\right] + 2\mu_I^2\Delta^2\left[-\frac{1}{g^2}+\frac{4N_{\rm c}}{(4\pi)^2}\ln\frac{M_l^2+\Delta^2}{M_0^2}\right] \tag{57}$$

and from s-quarks

$$\Omega_s = \frac{1}{2}\left(-\frac{m_M^2}{2g^2}M_s^2 + \frac{\lambda}{24g^4}M_s^4 - \frac{h_s}{g}M_s + \frac{2N_{\rm c}}{(4\pi)^2}M_s^4\left[\frac{3}{2}-\ln\frac{M_s^2}{M_0^2}\right]\right) \tag{58}$$

and the (u,d)-s quark mixing induced by the KMT interaction,

$$\Omega_{\rm mix} = -\frac{K}{g^3}\left(M_l^2+\Delta^2\right)M_s\,. \tag{59}$$

We note that, the strange quark sector shows the substantial μ_I dependence because of the $\mathrm{U}_A(1)$-induced coupling, $\sim\Delta^2 M_s$; the M_s increases as Δ does. The similar effects have been studied in the context of color superconductivity [61–64].

The expression of Ω is the renormalization group (RG) invariant for a given field values, provided that the renormalized masses, couplings, etc., follow the RG evolution. We have set the renormalization scale Λ to be the vacuum light quark mass, $M_0 \equiv M_l^{\rm vac}$, and then the couplings, etc., should be interpreted as those evaluated at $\Lambda = M_0$.

Finally, we mention that the expression is invalid for very large $g^2\ln\left(M^2+\Delta^2\right)$ [93]. As is well known, the one-loop effective potential is unbound for large field limits; there, we need higher orders in loops.

5.2. The Structure of the Gap Equations

The quark loops have added the logarithmic terms, which change the structure of the effective potential, especially at large μ_I. Let us see this assuming $M_l, M_s \ll \mu_I$. At the tree level, the effective potential behaves as

$$\Omega_{\rm tree} \;\to\; -\frac{2\mu_I^2}{g^2}\Delta^2 + \frac{\lambda}{24g^4}\Delta^4\,. \tag{60}$$

The gap equation for Δ balances the first and second terms, so $\Delta_{\rm tree} \sim \mu_I$ inevitably follows. Substituting back the solution $\Delta^2_{\rm tree} \sim 24\mu_I^2 g^2/\lambda$ into the $\Omega_{\rm tree}$, we find

$$\Omega_{\rm tree} \;\sim\; -\frac{24}{\lambda}\mu_I^4\,. \tag{61}$$

The hadronic parameter λ entirely fixes the coefficient of the μ_I^4 term.

This trend changes after including quark contributions. We assume that the gap equation leads to $M_{l,s}, \Delta \ll \mu_I$, and then check the consistency of this assumption (Figure 4). The large μ_I behavior of Ω is

$$\Omega \;\to\; \Omega_l^R + 2\mu_I^2\Delta^2\left[-\frac{1}{g^2} + \frac{4N_{\rm c}}{(4\pi)^2}\ln\frac{\Delta^2}{M_0^2}\right], \tag{62}$$

where the tree level terms, except μ_I^2/g^2 term, are suppressed compared to μ_I^2 and μ_I^4 terms. We note that the logarithmic contribution changes the sign at M_0; it becomes attractive contributions for $\Delta \lesssim M_0$ but repulsive for $\Delta \gtrsim M_0$. At large density, the latter stops the growth of Δ induced by the tree contribution before $\lambda\Delta^2$ terms are activated.

It turns out that Ω_l^R is well saturated by μ_I^4 terms and weakly depends on Δ. Then, the gap equation is dominated by the coefficients of μ_I^2 term as

$$\frac{\partial\Omega}{\partial\Delta^2} \;\to\; 2\mu_I^2\left[-\frac{1}{g^2} + \frac{4N_{\rm c}}{(4\pi)^2} + \frac{4N_{\rm c}}{(4\pi)^2}\ln\frac{\Delta^2}{M_0^2}\right] + O(M_0^2) \;\simeq\; 0\,. \tag{63}$$

This form with the logarithm is typical for low-dimensional systems; in the present case, the Fermi surface plays the role for the dimensional reduction. Unlike the tree level solution, at $M_0/\mu_I \to 0$, the gap does not manifestly contain the μ_I dependence,

$$\Delta^2 \simeq M_0^2\, {\rm e}^{-1+\frac{4\pi^2}{N_{\rm c}g^2}}\,. \tag{64}$$

The g dependence is a bit puzzling; the usual BCS-type calculations have the form of ${\rm e}^{-\#/G}$ with a coupling constant G, meaning that a stronger G increases the size of the gap. In contrast, a large g reduces the gap in our model. Our interpretation is the following: the condensed mesons at the tree level, where quarks inside are neglected, overreact to the increase in μ_I and become overpopulated as one can see from the scaling $\Delta_{\rm tree} \sim \mu_I$. In particular, the quark Pauli blocking is neglected. In light of this viewpoint, the explicit inclusion of quarks with the coupling to mesons should cancel the unwanted contributions and should temper the growth of Δ. This effect is stronger for a larger g. For a very small g, apparently Δ blows up, but then $\lambda\Delta^4$ terms become dominant and the situation goes back to the tree-level model or purely mesonic models. The philosophy here is in line with ref. [94] that introduced ghosts to cancel double counted contributions.

Substituting back the Δ into Ω, the thermodynamic potential at very large μ_I scales as

$$\Omega \;\sim\; \Omega_l^R - \frac{N_{\rm c}}{2\pi^2}\mu_I^2\Delta^2\,, \tag{65}$$

Note that, in Ω at large μ_I, the mesonic parameters m_M^2 and λ no longer play important roles, while the Yukawa coupling g is now hidden into the gap parameter Δ.

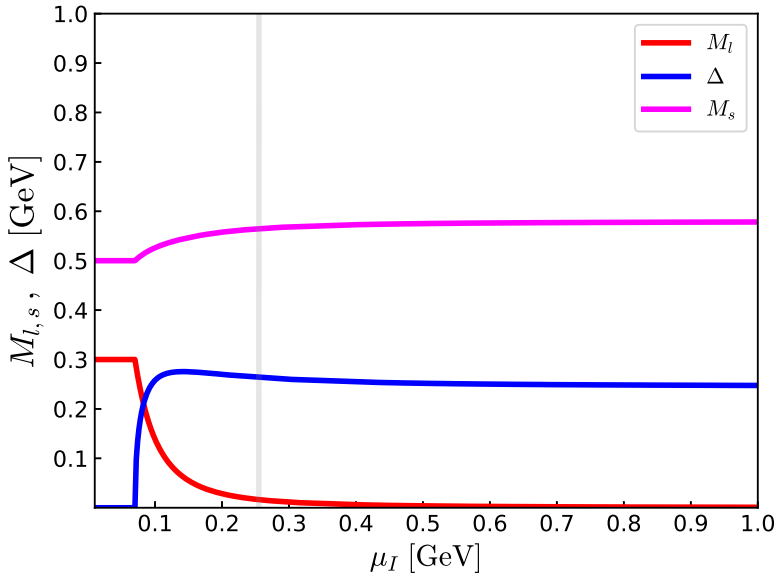

Figure 4. The effective quark masses M_l, M_s and the BCS gap Δ as functions of μ_I in the quark–meson model with the set B in Table 1. The growth in the strange quark mass comes from the $U_A(1)$ anomaly through which strange quarks couple to the pion condensate.

Table 1. The parameters in the quark–meson model (M_0, M_{s0} are given in GeV units). The parameters are chosen to reproduce the masses of the pseudo scalar nonet. We use the set B unless otherwise stated.

Set	M_0	M_{s0}	g	λ	m_M^2 [GeV^2]	h_l [GeV]	h_s [GeV]	K [GeV]
A	0.27	0.50	3.0	38.1	-0.269	1.82×10^{-3}	4.16×10^{-2}	1.2
B	0.30	0.50	3.3	42.4	-0.298	1.84×10^{-3}	4.19×10^{-2}	1.6
C	0.33	0.50	3.6	60.0	-0.278	1.85×10^{-3}	4.32×10^{-2}	2.0

6. Meson Poles at One-Loop: Parameter Fixing

Now we have all expressions needed to discuss EOS, but still the parameters in our model remain to be fixed. We use meson nonets in vacuum to fix our parameters. Here, the meson self-energies induced by quark loops must be taken into account for the consistency with the gap equations, Meanwhile, in this work, we do not address in-medium self-energies to meson masses.

6.1. Meson Poles

As we have constructed the effective potential at one loop, we need to upgrade the tree-level expressions of meson masses. This is essential to reproduce the masses of the Goldstone bosons which arise at the minima of the effective potential at a given order of approximation. The analyses go as in the Nambu–Jona–Lasinio model [95].

An inverse of the meson propagator with loops takes the form

$$-p^2 + m^2 = -p^2 + m^2_{\rm tree} + \Sigma^q(m^2) + \Sigma^{c.t.}(m^2)\,, \tag{66}$$

where Σ^q comes from quark loops, while $\Sigma^{c.t.}$ from the counter terms. In the case of pions, we have

$$-p^2 + m_\pi^2 = \left(-m_M^2 + \frac{\lambda}{2g^2} M_0^2 - 2\frac{K}{g} M_s \right) + \Sigma_\pi^q(m_\pi^2) - p^2 \delta Z_\phi + \frac{\delta\lambda}{2g^2} M_0^2\,. \tag{67}$$

We obtained the counter terms from the tree-level bare parameters.

It is convenient to define

$$\begin{aligned}\Sigma^q_{fg}(p^2) &= \mathrm{i}g^2 \int_l \mathrm{tr}_{\mathrm{c,D}}\left[S_f(l)\mathrm{i}\gamma_5 S_g(p+l)\mathrm{i}\gamma_5\right] \\ &= \frac{2g^2N_\mathrm{c}}{(4\pi)^2\epsilon}\left[M_f^2+M_g^2+\left[\,(M_f-M_g)^2-p^2\,\right]\right] \\ &\quad + \frac{2g^2N_\mathrm{c}}{(4\pi)^2}\left[M_f^2+M_g^2+M_f^2\ln\frac{\Lambda^2}{M_f^2}+M_g^2\ln\frac{\Lambda^2}{M_g^2}+\left[\,(M_f-M_g)^2-p^2\,\right]\mathcal{B}_{fg}(p^2)\right], \quad (68)\end{aligned}$$

with a function including the Feynman parameter,

$$\mathcal{B}_{fg}(p^2) \equiv \int_0^1 \mathrm{d}x\ \ln\frac{\Lambda^2}{(1-x)M_f^2+xM_g^2-p^2x(1-x)}\,. \quad (69)$$

This logarithm in the integral can be negative for $p^2 > (M_f+M_g)^2$ and $p^2 < (M_f-M_g)^2$. (Actually, the latter regime does not occur for $0 \le x \le 1$.) In such a case, the imaginary part appears as $\ln(-y-\mathrm{i}\epsilon) \to \ln|y| - \mathrm{i}\pi$. The imaginary part describes the decay of mesons into constituent quarks, but this is supposed to be an artifact of not taking account the quark confinement. Realistically, a meson decays into mesons, and the width is typically smaller than the mass, except for some scalar mesons. For simplicity, in this work, we estimate a meson mass as the location where the real part becomes zero. Also, we discuss the mixing between the flavor singlet and octet using the real part only.

Remember that we chose $\Lambda = M_0$ for the effective potential, so we do the same in the following. For the pseudoscalar channels,

$$\begin{aligned}&\Sigma^q_\pi = 2\Sigma^q_{ll}\,, \quad \Sigma^q_K = 2\Sigma^q_{ls}\,, \\ &\Sigma^q_{00} = \frac{2}{N_\mathrm{f}}\left(2\Sigma^q_{ll}+\Sigma^q_{ss}\right), \quad \Sigma^q_{88} = \frac{2}{N_\mathrm{f}}\left(\Sigma^q_{ll}+2\Sigma^q_{ss}\right), \quad \Sigma^q_{08} = \frac{2\sqrt{2}}{N_\mathrm{f}}\left(\Sigma^q_{ll}-\Sigma^q_{ss}\right), \quad (70)\end{aligned}$$

Moreover, to obtain similar expressions for the scalar channel, we can simply replace $(M_f-M_g)^2$ with $(M_f+M_g)^2$.

Let us see some examples. For pions

$$\Sigma^q_\pi(p^2) = \frac{4g^2N_\mathrm{c}}{(4\pi)^2\epsilon}\left(2M_0^2-p^2\right) + \frac{4g^2N_\mathrm{c}}{(4\pi)^2}\left(2M_0^2-p^2\,\mathcal{B}_{ll}(m_\pi^2)\right). \quad (71)$$

Combining this expression with the counter term $\Sigma^{c.t.}_\pi$, the UV divergence proportional to M_0^2 is canceled by the previously determined $\delta\lambda$. The divergence coupled to p^2 can be canceled by choosing

$$\delta Z_\phi = -\frac{4g^2N_\mathrm{c}}{(4\pi)^2\epsilon}\,. \quad (72)$$

Below, we write $\Sigma = \Sigma^q + \Sigma^{c.t.}$ for the renormalized self-energy. The pole condition for pions is $m_\pi^2 = \left(m_\pi^{\mathrm{tree}}\right)^2 + \Sigma_\pi(m_\pi^2)$ with

$$\Sigma_\pi(m_\pi^2) = \frac{4g^2N_\mathrm{c}}{(4\pi)^2}\left(2M_0^2-m_\pi^2\,\mathcal{B}_{ll}(m_\pi^2)\right). \quad (73)$$

For kaons, the above chosen counter terms cancel the divergence in the kaon self-energy, leaving the condition $m_K^2 = \left(m_K^{\mathrm{tree}}\right)^2 + \Sigma_K(m_K^2)$ with

$$\Sigma_K(m_K^2) = \frac{4g^2N_\mathrm{c}}{(4\pi)^2}\left(M_0^2+M_{s0}^2+M_{s0}^2\ln\frac{M_0^2}{M_{s0}^2}+\left[(M_0-M_{s0})^2-m_K^2\right]\mathcal{B}_{ls}(m_K^2)\right). \quad (74)$$

We do the same for 00, 88, and 08 channels, which are to be diagonalized to yield the η and η' spectra. The η and η' masses are found by searching p^2 satisfying

$$\det\begin{bmatrix} -p^2+(m_{00}^{\rm tree})^2+\Sigma_{00}(p^2) & (m_{08}^{\rm tree})^2+\Sigma_{08}(p^2) \\ (m_{80}^{\rm tree})^2+\Sigma_{80}(p^2) & -p^2+(m_{88}^{\rm tree})^2+\Sigma_{88}(p^2) \end{bmatrix}=0\,. \tag{75}$$

The mixing is induced by the flavor breaking associated with $M_l - M_s$. It is worth mentioning that the mixing angle depends on the energy, not a constant [95].

6.2. Parameter Fixing

We have $(g, m_M^2, \lambda, K, h_l, h_s, M_0, M_{s0})$ for our parameters. We treat M_0 and M_{s0} as our input parameters, and set

$$M_0 = 0.3\ \text{GeV}\,, \quad M_{s0} = 0.5\ \text{GeV}\,. \tag{76}$$

Next, we fix h_l and h_s so that the minima of the effective potential in vacuum are found at $M_l = M_0$ and $M_s = M_{s0}$,

$$\left.\frac{\partial\Omega}{\partial M_l}\right|_{M_l=M_0,\,M_s=M_{s0}} = \left.\frac{\partial\Omega}{\partial M_s}\right|_{M_l=M_0,\,M_s=M_{s0}} = 0\,. \tag{77}$$

The leftover parameters are (g, m_M^2, λ, K). We have four meson spectra $(m_\pi, m_K, m_\eta, m_{\eta'}) \simeq (0.14, 0.50, 0.55, 0.96)$ GeV, so the four parameters can be fixed. Here, we use the pseudo-scalar mesons for the parameter fixing instead of using σ mesons since the nature of σ mesons is more uncertain than the pseudo-scalar mesons. The results are summarized in Tables 1 and 2. The σ and η' masses are sensitive to the value of K; m_σ is reduced, while $m_{\eta'}$ is enhanced by the anomaly. Here, we include the spectra of scalar mesons just because we can compute them. As is well known, however, scalar mesons are not well described by simple valence quark states and indeed the agreement between our model and experimental results is not good especially for a_0 mesons which, together with the isosinglet $f_0(980)$, are often regarded as $K\bar{K}$ molecules.

Table 2. The masses of the pseudo scalar and scalar nonets with the experimental masses indicated in the parenthesis (experimentally, the σ and κ have the width of $\sim$500 MeV).

Set	m_π**(138)**	m_K**(496)**	m_η**(548)**	$m_{\eta'}$**(958)**	m_σ**(500*)**	m_{a_0}**(980)**	m_κ**(700*)**
A	0.14	0.50	0.52	0.97	0.51	0.67	0.75
B	0.14	0.50	0.54	0.97	0.54	0.73	0.80
C	0.14	0.50	0.55	0.95	0.64	0.81	0.88

7. Equations of State at Zero Temperature

We examine equations of state. Substituting the solutions of gap equations into Ω, the thermodynamic potential is $P = -\Omega$. The isospin density is

$$n_I \equiv \frac{\tilde{n}_I}{2} = \frac{1}{2}\frac{\partial P}{\partial \mu_I}\,. \tag{78}$$

As we mentioned before, we define $\mu_I (= \mu_u = -\mu_d)$ in an unconventional way to simplify the notation. For physical interpretation, we should use n_I, rather than $\tilde{n}_I$, which is directly derivable from the derivative of P. The energy density is $\varepsilon = \mu_I \tilde{n}_I - P$.

At low density, the condensate is driven by pions with $I_3 = 1$; as far as isospin density is saturated by those pions, one can interpret the isospin density as the pion density $n_I \simeq n_\pi$. A good measure to estimate the density where pions overlap is

$$n_\pi^{\rm overlap} \equiv \left(\frac{4\pi r_\pi^3}{3}\right)^{-1} \simeq 0.83\,{\rm fm}^{-3} \simeq 5.2 n_0\,, \tag{79}$$

where we introduced $n_0 = 0.16\,{\rm fm}^{-3}$ as a unit frequently used in nuclear physics. The estimate utilizes the root-mean-square radius of a pion, $r_\pi \simeq 0.66$ fm, in vacuum [96–99]. The size of a pion is comparable to that of a nucleon; the nucleon charge root-mean-square radius is $\simeq$0.84 fm, while its mass radius based on the gravitational form factor [100] is $\simeq$0.55 fm [101], or the "valence quark core radius" is $\simeq$0.5 fm [102]. The relation between μ_I and n_I is shown in Figure 5. The overlap density $n_\pi^{\rm overlap}$ is reached at a low chemical potential $\mu_I \simeq 0.256$ GeV.

A useful quantity characterizing the rapid stiffening is the sound speed. A matter is called stiff (soft), i.e., P is large (small) at a given ε, and its variation is reflected in c_s^2. Writing the susceptibility as $\tilde{\chi} = \partial^2 P/\partial \mu_I^2$, the sound speed is given by

$$c_s^2 = \left.\frac{{\rm d}P}{{\rm d}\varepsilon}\right|_{s=0} = \frac{\tilde{n}_I {\rm d}\mu_I}{\mu_I {\rm d}\tilde{n}_I} = \frac{\tilde{n}_I}{\mu_I \tilde{\chi}_I}\,. \tag{80}$$

The result of the quark–meson model is shown in Figure 6. The c_s^2 grows quickly just after the onset of the pion condensation, makes a peak before n_I reaching $n_\pi^{\rm overlap}$, and slowly relaxes to the conformal limit 1/3. The result is compared with the lattice results of Brandt et al. [22] which have more focus on low density and those of Abbott et al. [21], which study the global structure for a wider range of μ_I. The results are consistent. Later, we delineate the behavior of c_s^2 at low and high densities from the microphysics viewpoint.

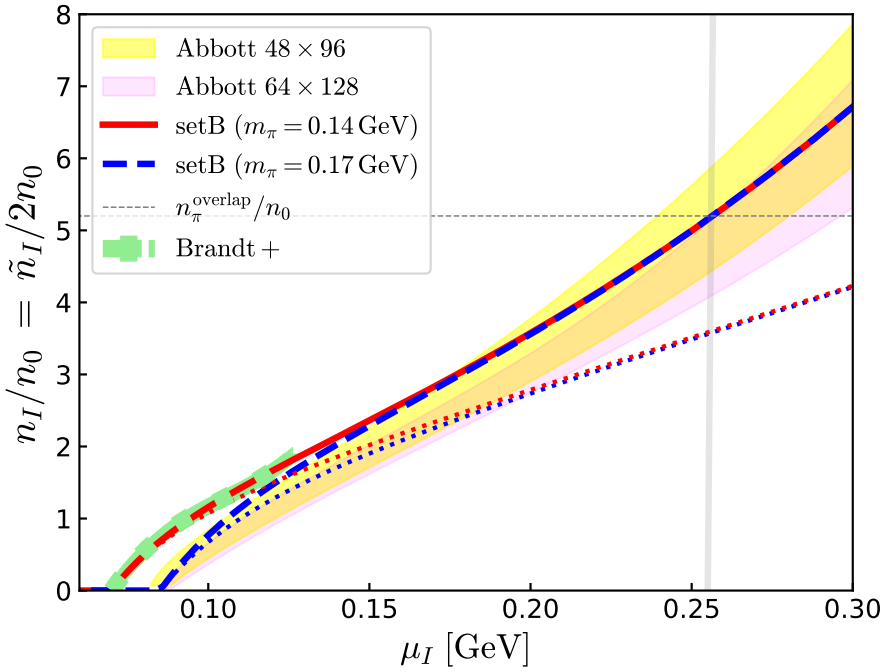

Figure 5. The isospin density $n_I/n_0 (= \tilde{n}_I/2n_0)$ as a function of μ_I. The results of the quark–meson model for $m_\pi = 0.14$ GeV and $m_\pi = 0.17$ GeV are compared with the lattice data by Brandt et al. [22] and Abbott et al. [21], respectively. The overlap density $n_\pi^{\rm overlap} \simeq 5.2 n_0$ which is achieved at $\mu_I \simeq 0.256$ GeV is shown as a guide. The red and blue dotted curves are from the leader order ChPT for $m_\pi = 0.14$ and 0.17 GeV, respectively.

Recently, the trace anomaly of EOS has attracted attention [70,103–105]. It is one of hot topics for forthcoming electron ion collider experiments which will explore the nucleon structure in great detail. The trace anomaly normalized by 3ε [103],

$$\Delta_{\rm tr} \equiv \frac{\langle T^\mu_\mu \rangle}{3\varepsilon} = \frac{1}{3} - \frac{P}{\varepsilon} \tag{81}$$

is a useful measure for the deviation from the conformal limit. The result is shown in Figure 7. In the non-relativistic limit, $P \ll \varepsilon$, the $\Delta_{\rm tr} = 1/3$. In the conformal limit, $\Delta_{\rm tr} = 0$. When $\Delta_{\rm tr} < 0$, there should be strong correlation effects. Below, we discuss the power corrections as candidates to drive $\Delta_{\rm tr}$ to the negative value.

As a guide for the low-density behaviors, it is useful to quote the results from the chiral perturbation theory (ChPT),

$$P = 2f_\pi^2 \mu_I^2 \left(1 - \frac{m_\pi^2}{2\mu_I}\right)^4, \tag{82}$$

which leads to

$$n_I = \frac{\tilde{n}_I}{2} = 2f_\pi^2 \mu_I \left[1 - \left(\frac{m_\pi}{2\mu_I}\right)^4\right], \qquad c_s^2 = \frac{(2\mu_I)^4 - m_\pi^4}{(2\mu_I)^4 + 3m_\pi^4}. \tag{83}$$

At large density, the sound speed asymptotically approaches $c_s^2 = 1$. Here, the scaling $\varepsilon \sim n_I^2$ holds; the system is as if it is dominated by repulsive two-body forces.

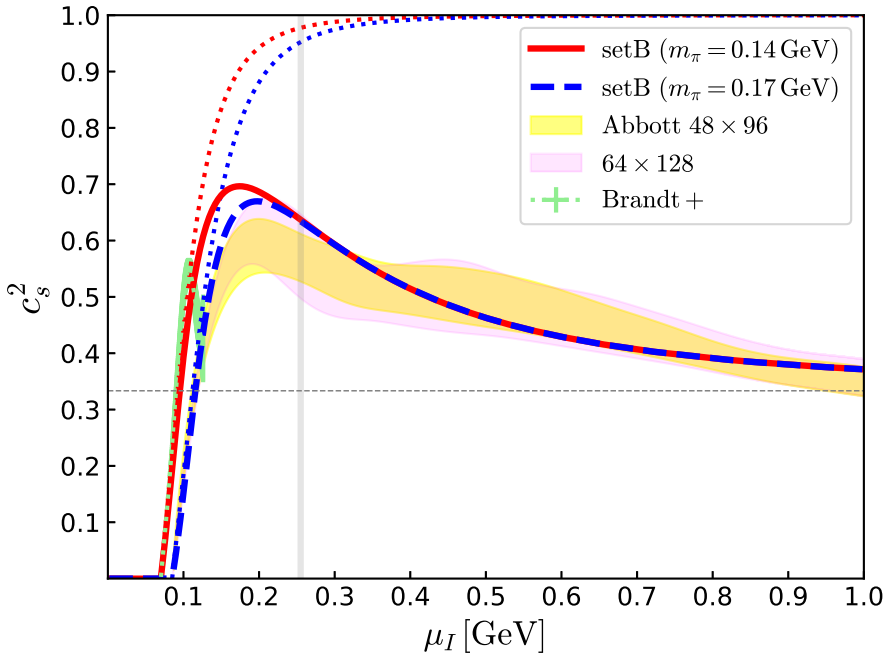

Figure 6. The sound speed as a function of μ_I. The results of the quark–meson model for $m_\pi = 0.14$ GeV and $m_\pi = 0.17$ GeV are compared with the lattice data by Brandt et al. [22] and Abbott et al. [21], respectively. The conformal value $c_s^2 = 1/3$ and the ChPT results (dotted curves) are also shown as guides.

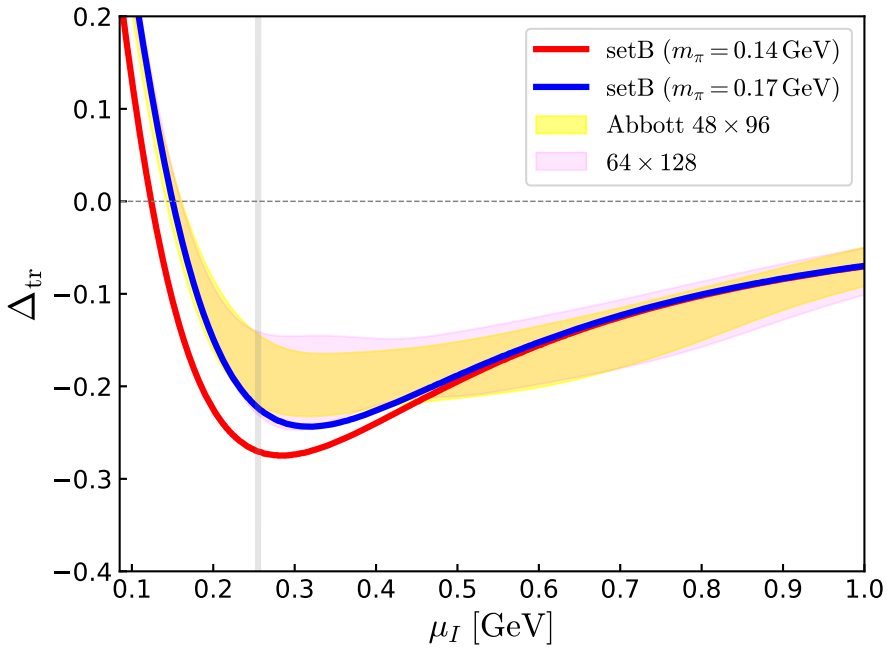

Figure 7. The trace anomaly Δ_{tr} for the same setup as Figure 6. The conformal limit is $\Delta_{\mathrm{tr}} = 0$.

7.1. High-Density Regime: Conformal Behaviors

Let us first consider the high-density regime in our model and the effective degrees of freedom. In the conformal limit with no mass scale other than μ_I, the dimensional analyses lead to

$$\frac{\partial(P/\mu_I^4)}{\partial \mu_I} = 0 \quad \to \quad P = \frac{\varepsilon}{3}\,. \tag{84}$$

This relation is approximately satisfied in the high-density limit, where the kinetic energy dominates over mass and interaction energies. (Strictly speaking, there are self-energies that do not necessarily die out at high energy; in QCD, the asymptotic freedom guarantees the self-energies become weaker at high energy.)

The conformal limit by itself does not tell which degrees of freedom are relevant. Indeed, supposing $P \simeq a\mu_I^4$, the conformal limit is obtained for whatever value of a; we have to specify a to tell which degrees of freedom dominate. As we saw, the tree-level pressure includes only mesonic degrees of freedom, and the one-loop pressure (dominated by quark degrees of freedom) scales as

$$P_{\mathrm{tree}} \sim \frac{24}{\lambda}\mu_I^4\,, \qquad P_{1-\mathrm{loop}} \sim \frac{N_{\mathrm{f}}^{\mathrm{eff}} N_{\mathrm{c}}}{12\pi^2}\mu_I^4\,, \tag{85}$$

where $\mu_I = \mu_u = -\mu_d$ and we should substitute $N_{\mathrm{f}}^{\mathrm{eff}} = 2$. In order for the former to reproduce the latter, we need $\lambda \simeq 474$, which is unacceptably large. For P_{tree}, the $\Delta_{\mathrm{tree}} \sim \mu_I g/\sqrt{\lambda}$ plays an essential role for the conformal scaling, and its magnitude is determined by details of interactions. In stark contrast, the conformal scaling of $P_{1-\mathrm{loop}}$ is determined by the number of quark degrees of freedom and is robust to the interactions.

7.2. High-Density Regime: Perturbative and Power Corrections

Next, we consider corrections to the conformal limit. The most frequently and rigorously discussed is the perturbative corrections at the weak coupling regime. The perturbative corrections modify the coefficient of μ_I^4 term by adding series of $\alpha_s(\bar{\Lambda})$, where $\bar{\Lambda}$ is the renormalization scale to be set to the natural scale for a given problem. At large density,

$\bar{\Lambda} \sim \mu_I$ is the natural choice. The intrinsic scale of QCD, $\Lambda_{\rm QCD} \simeq 200$–$300$ MeV, appearing only through α_s, shows up in the form of $\sim\ln(\mu_I/\Lambda_{\rm QCD})$. To the one-loop β-function,

$$\frac{\partial \alpha_s(\mu_I)}{\partial \ln \mu_I} = -\frac{11N_{\rm c} - 2N_{\rm f}}{24\pi}\alpha_s^2\,, \qquad N_{\rm f} = 3\,. \tag{86}$$

This reduces P, n_I, and c_s^2 from the conformal value. At asymptotic density, the c_s^2 approaches the conformal limit from below.

In addition, in QCD, there are power corrections in powers of $\Lambda_{\rm QCD}/\mu_I$. This sort of term cannot be expressed by powers of series of α_s,

$$\Lambda_{\rm QCD}^{1-\rm loop} \simeq \mu_I {\rm e}^{-2\pi/\beta_0\alpha_s(\mu_I)}\,, \qquad \beta_0 = 11 - 2N_{\rm f}/3\,. \tag{87}$$

and hence is non-perturbative. For the momentum transfer of $\sim\Lambda_{\rm QCD}$, quarks are supposed to strongly interact.

Actually, whether such soft interactions are important or not depends on the presence of the color screening. If the screening is strong in the infrared, soft interactions are cut off. In the case of the pion-condensed phase, the condensate is a color-singlet and produces a gap for a quark–hole excitation. This suppresses the Debye and Meissner screening. Hence the electric and magnetic color interactions can be as strong as in the vacuum until the phase space factor $\sim 4\pi\mu_I^2$ overwhelms the suppression factor by the gap.

Adding the power corrections can change the qualitative behavior of c_s^2 [50,106–110]. In particular, the power corrections adding positive contributions to the pressure favors the trend opposite to those from perturbative corrections, and hence can be thought of a clear indicator for non-perturbative physics in the high-density domain. For a simple parametrization [50]

$$P = a\left(\mu_I^4 + c_2\Delta^2\mu_I^2\right) - B\,, \tag{88}$$

with $a, c_2 > 0$ being dimensionless constants and B included for normalization, we find

$$\tilde{n}_I = 2a\left(2\mu_I^3 + c_2\Delta^2\mu_I\right)\,, \quad \tilde{\chi}_I = 2a\left(6\mu_I^2 + c_2\Delta^2\right)\,, \tag{89}$$

with which

$$c_s^2 = \frac{2\mu_I^2 + c_2\Delta^2}{6\mu_I^2 + c_2\Delta^2} = \frac{1}{3} + \frac{2}{3}\frac{c_2\Delta^2}{6\mu_I^2 + c_2\Delta^2}\,, \tag{90}$$

varying between $1/3$ and 1. In our quark–meson model $a = N_{\rm c}/6\pi^2$, $c_2 \simeq 3$, and $\Delta \simeq 0.25$–0.3 GeV [50]. The power corrections of $O(10\%)$ to the pressure occurs when

$$3(\Delta/\mu_I)^2 \sim 0.1 \;\to\; \mu_I \sim 1.6\ {\rm GeV} \times \frac{\Delta}{0.3\ {\rm GeV}}\,, \tag{91}$$

where the corrections increase c_s^2 as $0.333 \to 0.344$ for $\Delta \simeq 0.3$ GeV. The non-perturbative effects would survive at a relatively high density of $\mu_I \sim 1$ GeV. These analyses, although still crude, indicate that the convergence of α_s expansion at high density, which seems to be universal, may not be sufficient to judge the relevance/irrelevance of the non-perturbative physics.

The lattice results for EOS by Abbott et al. [21] to $\mu_I \sim 1.7$ GeV (μ_I defined in our work is a half of theirs) show qualitative deviation from perturbative QCD predictions. One of the plausible sources is the power corrections from the $\sim\mu_I^2\Delta^2$ terms, where Δ is non-analytic in the strong coupling constant g_s. This indicates that non-perturbative physics can survive to a very high density, even where $\alpha_s(\mu_I)$ is reasonably small [50]. Recently, ref. [21] used the deviation between the perturbative EOS and lattice results to

estimate the size of the BCS gap in the weak coupling region $\mu_I \in [0.750, 1.625]$ GeV [20]. The expression used for the EOS is [52]

$$\delta P = P(\Delta) - P(\Delta = 0) = \frac{N_c}{2\pi^2}\mu_I^2\Delta^2\left(1 + \frac{g_s}{6}\right). \tag{92}$$

The lattice results show that Δ increases toward the low-density region. Meanwhile, the gap estimated by the weak coupling method is

$$\Delta = \tilde{b}\mu_I \exp\left[-\frac{\pi^2+4}{16}\right]\exp\left[-\frac{3\pi^2}{2g_s}\right], \qquad \tilde{b} = 512\pi^4 g_s^{-5}, \tag{93}$$

which is sensitive to the choice of the running $g_s(\bar{\Lambda})$. The estimates with $\bar{\Lambda} = \mu_I$ and $2\mu_I$ cover the range consistent with those estimated from the lattice results and Equation (92). On the other hand, the μ_I dependence looks the opposite; the gap of Equation (93) decreases toward the low-density region. We conjecture that the physics of soft gluons and quarks enhances the gap and cures the discrepancy.

The power corrections also play important roles in the trace anomaly. In the parametrization Equation (88), the energy density is

$$\varepsilon = a\left(3\mu_I^4 + c_2\Delta^2\mu_I^2\right) + B, \tag{94}$$

so that

$$\langle T^\mu_\mu \rangle = \varepsilon - 3P = -2ac_2\Delta^2\mu_I^2 + 4B. \tag{95}$$

Remarkably, the power corrections yield negative contributions. Meanwhile, the normalization (bag) constant measures the energy difference between the conformal and non-perturbative vacuum and should be $\sim\Lambda_{\rm QCD}^4$ and positive. Perturbative corrections not written here also give positive contributions [50]. Hence, the negative trace anomaly can be regarded as a good indicator for the importance of the non-perturbative physics in dense matter.

7.3. Quark Saturation

Finally, we try to characterize EOS through quarks inside of pions. At sufficiently low density, quarks should show up only as constituents of pions. Pion condensation generates BCS gaps for quarks with which quark contributions can become finite even for $\mu_I (= \mu_u = -\mu_d) < M_l$; see the structure of Equation (49). In the pion-condensed phase, the occupation probability of $u, \bar{d}$ quark states can be written as

$$f_Q(p; n_I) \equiv f_{u,\bar{d}}(p; n_I) = \frac{1}{2}\left(1 - \frac{E_l - \mu_I}{\sqrt{(E_l - \mu_I)^2 + \Delta^2}}\right), \tag{96}$$

which becomes $\Theta(\mu_I - E_l)$ for $\Delta \to 0$. The behavior of $f_Q(p)$ as a function of p for various n_I is shown in Figure 8 for the parameter set B.

As quarks are bound to a compact object, the quark momentum distribution is broad in momentum. In particular, the occupation probability at $p = 0$ is substantially smaller than 1. As the density increases, the magnitude of f_Q becomes larger. If we neglect the interactions and the structural changes of pions, we would find the scaling

$$f_Q^{\rm id}(p; n_I) \equiv n_I \frac{\partial f_Q(p; n_I)}{\partial n_I}\bigg|_{n_I=0}, \tag{97}$$

where pions condense into the zero momentum state; each pion gives the same quark contribution and hence simply scale as $\sim n_I$. Obviously, extrapolating this expression

would violate the Pauli exclusion principle for quarks, $f_Q(p) \leq 1$ for any p. We define the "(pseudo-)quark-saturation" density $n_I^{\rm id}$ as

$$1 = f_Q^{\rm id}(p = 0; n_I^{\rm id}), \tag{98}$$

and use $n_I^{\rm id}$ as the characteristic measure, where either pion interactions or quark saturation constraints become important.

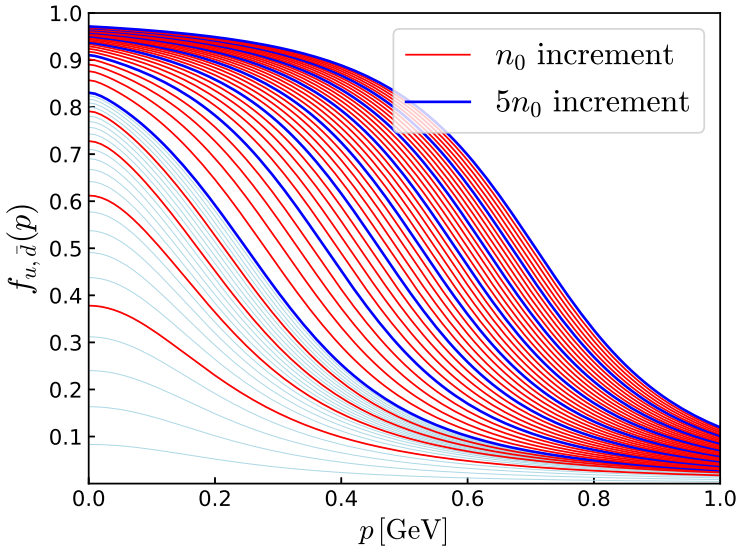

Figure 8. The occupation probability $f_{u,\bar{d}}(p)$ as a function of p for the parameter set B in Table 1. Red curves represent curves for n_0 increments, $n_0, 2n_0, \cdots$ while blue curves represent those for $5n_0$ increments. To $5n_0$, we also show thin light blue curves for $0.2n_0$ increments. The figure covers up to $n_I = 20n_0$.

Figure 9 shows $f_Q(p = 0; n_I)$ as a measure of the quark saturation. We also show the $f_Q^{\rm id}$ with dashed lines to examine $n_I^{\rm id}$. To examine how $n_I^{\rm id}$ depends on the compactness, we vary M_0 to change the binding energy of a pion, $2M_0 - m_\pi$, while maintaining the spectra of pseudo-scalar nonets within a reasonable range. Concretely, we compare the set A-C in Table 1. With a larger M_0, the $n_I^{\rm id}$ is larger, as the pion is spatially more compact and has a broader quark momentum distribution. For $M_0 = (0.27, 0.30, 0.33)$ GeV, we find $n_I^{\rm id} \simeq (2.2, 2.4, 2.6)n_0$, respectively. These densities are substantially smaller than the $n_\pi^{\rm overlap} \simeq 5.2n_0$.

In principle, by specifying f_Q and gaps $(M_l\,, \Delta\,, M_s)$ at a given μ_I, one can reconstruct the corresponding EOS as

$$P(\mu_I) = \int_0^{\mu_I} {\rm d}\mu' n_I(\mu') = \int_0^{\mu_I} {\rm d}\mu' \int_p \sum_f \left[f_Q(p; \mu') - f_{\bar{Q}}(p; \mu') \right], \tag{99}$$

and hence, the evolution of f_Q (and $f_{\bar{Q}}$ for antiparticles) contains sufficient information to study the EOS.

Shown in Figure 10 are the behaviors of M_l and Δ at several densities and M_0. For a greater M_0, the gap Δ is naturally larger. As guides, we display $n_I^{\rm id}$ using several vertical lines. The general tendency is that, beyond $n_I^{\rm id}$, the gap becomes insensitive to μ_I , reflecting that the gap equations are dominated by soft gluon and soft quark contributions. The parameter set A-C leads to the gap of ∼0.23–0.28 GeV around $\mu_I \sim 1$ GeV. Hard gluon contributions, which are omitted in this work, should further enhance the size of the gap and introduce the stronger μ_I dependence, as it is sensitive to the phase space around the Fermi surface.

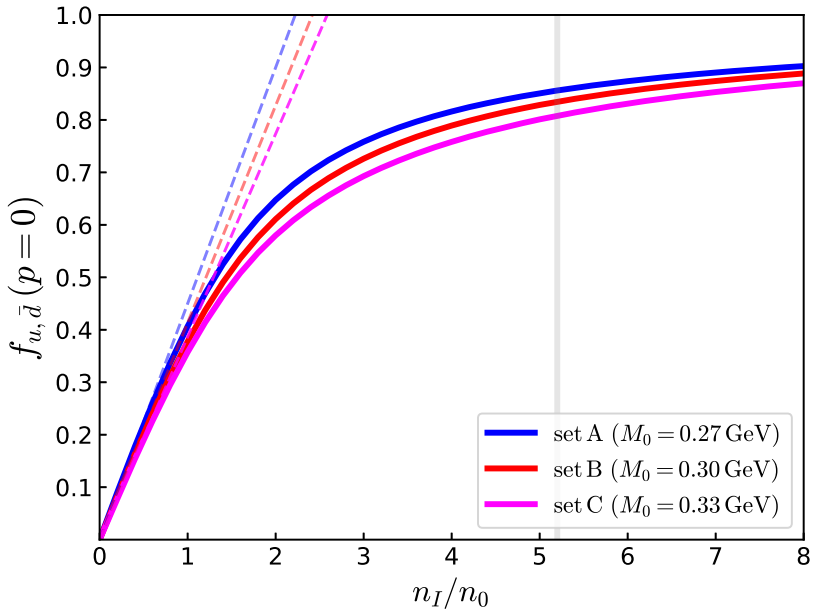

Figure 9. The occupation probability at zero momentum, $f_{u,\bar{d}}(p = 0)$ at various n_I/n_0. With the parameter sets A–C, we vary $M_0 (= M^{\rm vac}_{u,\bar{d}})$ to change the "binding energies" for quarks to form pions; a larger M_0 has the stronger binding $\sim 2M_0 - m_\pi$ and leads to a more spatially compact state. The dashed curves are a linear extrapolation of the low-density behavior $f^{\rm id}_{u,\bar{d}}(n_I) \equiv n_I \partial f_{u,\bar{d}}(p=0)/\partial n_I|_{n_I=0}$, which characterizes the $f_{u,\bar{d}}$ for non-interacting pions. We also show $n_\pi^{\rm overlap}$ as a guide.

Finally, in Figure 11 we examine the sound speed for varying M_0. For smaller M_0, the rising of c_s^2 occurs at a lower density. This is natural, as pions are less compact objects. Increasing M_0 delays the rising of c_s^2. The structure of a hadron, its valence core size, and quantum fluctuations around it [111] have direct relevance to the stiffening of matter. The relation between the baryon structure and nuclear matter has been discussed in refs. [112–115].

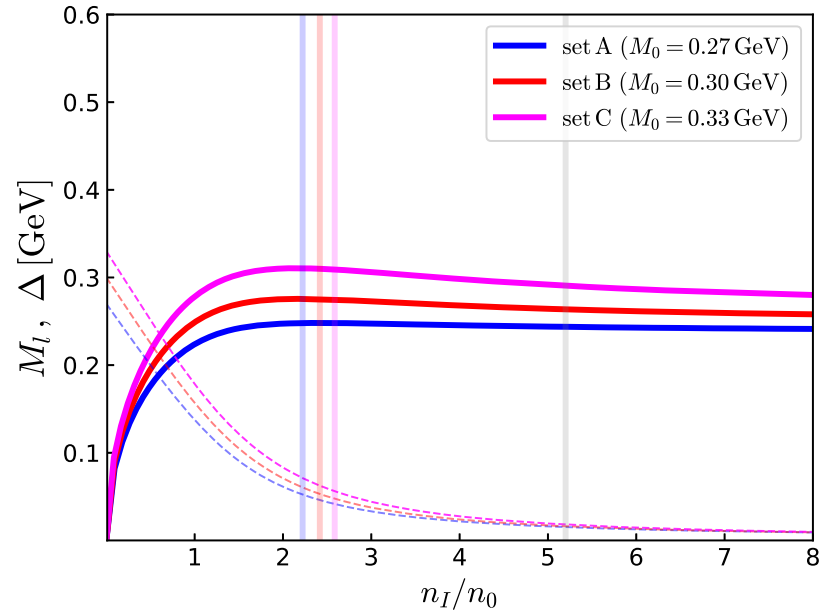

Figure 10. Behaviors of M_I (dashed lines) and Δ (solid lines) for the same parameter set as Figure 9. The vertical lines with various colors represent the $n_I^{\rm id}$ defined in Equation (98) for the set A, B, and C.

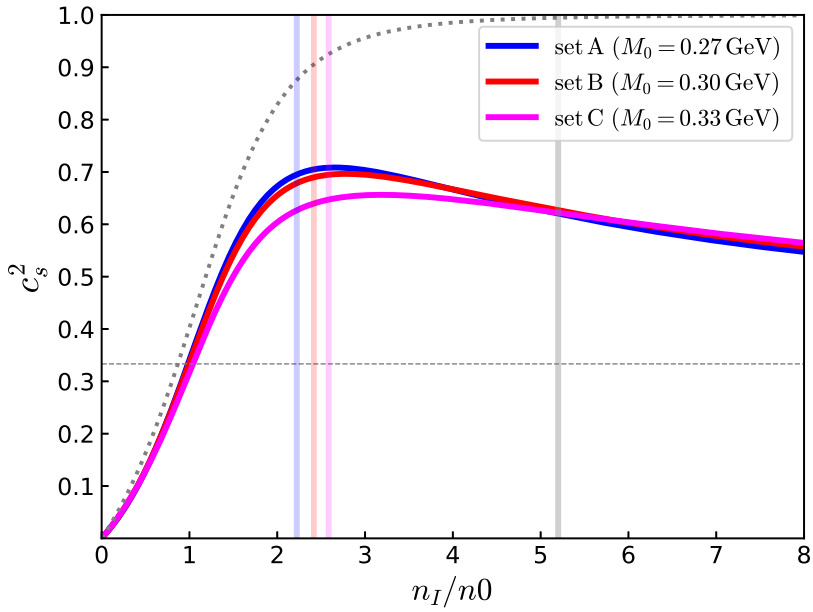

Figure 11. The sound speed as a function of n_I/n_0 for the same parameter set as Figure 9. When pions are more spatially compact ($2M_0 - m_\pi$ is larger), the repulsion among pions or quark saturation effects set in at larger densities.

8. Summary

In this paper, we study the EOS of isospin QCD and its relationship to the microphysics. We used a quark–meson model that interpolates the hadronic and quark sector at microscopic level. While it is difficult for such model studies to avoid model dependence to some degree, instead they can clarify the microphysics which is manifestly taken into account by studies based on the interpolation of ChPT and perturbative computations supplemented by astrophysical constraints. Among several effective models such as Nambu–Jona–Lasinio-type models, the quark–meson model is more useful, as it is renormalizable so that it can be used to cover from low to high densities, at least formally. Although the model does not cover the aspects of QCD caused by hard gluons, it captures some aspects of the physics caused by soft gluons in a parametrized manner.

One of the important issues in dense QCD is how non-perturbative effects relevant in hadron physics die out. Recent lattice results for EOS [21] to $\mu_I \sim 1.7$ GeV (μ_I defined in our work is a half of theirs) indicate the importance of the power corrections from the $\sim \mu_I^2 \Delta^2$ terms with Δ being non-analytic in the QCD coupling constant g_s, even at high density, where $\alpha_s(\mu_I)$ is reasonably small [50]. Concerning the size of the gap, there are several questions to be answered. The first question is at which density the evaluation of the gap is closed within the weak coupling regime; in the weak coupling estimates, we assume that hard momentum transfer processes dominate the gap equation because of the large phase space. This mechanism is sensitive to the density, and at low density, soft gluons should become important. How the transition between these two regimes occurs is directly related to the reliability of various estimates. The second question is to what extent the extrapolation from isospin QCD to QCD at finite baryon density can be valid. The mechanism for the emergence of the BCS gap is the diquark condensates in the color superconductivity. The typical estimate for the gap, mostly based on the weak coupling picture, is $\Delta \lesssim 100$ MeV; the coefficient of $1/g_s$ in the weak coupling expression of gap is larger than in the isospin QCD so that the gap is smaller. Analyses predicting a greater gap are mostly based on effective models constrained by hadron physics. It is important to fill the gap between the two regimes.

The quarks in pions seem important before reaching the overlap density for pions, $n_\pi^{\text{overlap}} \simeq 5.2 n_0$, which is inferred from the size of a pion in vacuum. Even if we neglect

the structural change of pions such as swelling or dissociation, we cannot go much beyond $\sim 0.5 n_\pi^{\rm overlap} \simeq 2.6 n_0$ neglecting constraints from the quark Pauli blocking. The sound speed peak is also found around $\sim 0.5 n_\pi^{\rm overlap}$. If the quark exchange interactions (or meson exchange) among pions effectively increase the size of pions, quark states at low momenta become saturated more quickly, inducing the Pauli blocking effects even earlier. The quark Pauli blocking near hadronic matter should also give insights on many-body forces among hadrons. In the context of neutron star EOS, it is typical to utilize two- and three-body repulsion to satisfy the two-solar mass constraints. But in such descriptions, there always remains a question of how to handle the convergence of many-body forces. We need an organizing principle. We guess that the quark saturation effects do the job.

Analyses in this paper left several important problems. In the methodology, we should improve the one-loop results. Another important topic is the meson spectra at finite density, including quark loops. We have computed the meson spectra in vacuum for the parameter fixing but have not performed analyses at finite density. The latter is necessary to answer to interesting questions such as how mesons dissociate and change the structure. How mesons or quarks in medium contribute to the entropy is also important to understand the color confinement at finite density, a question originally posed in the quarkyonic matter hypothesis [116]. The analyses toward this issue are in progress.

Author Contributions: Conceptualization, T.K., D.S. and R.C.; formal analysis, T.K. and R.C.; writing—original draft preparation, T.K.; writing—review and editing, T.K. and D.S. All authors have read and agreed to the published version of the manuscript.

Funding: T.K. was supported by JSPS KAKENHI Grant No. 23K03377 and No. 18H05407, and by the Graduate Program on Physics for the Universe (GPPU) at Tohoku university; D.S. by JSPS KAKENHI Grant No. 23H05439.

Data Availability Statement: The data is provided upon request.

Acknowledgments: We thank Bastian B. Brandt and Gergely Endrődi for kindly providing us with their lattice data in Ref. [22], and Ryan Abbott and his collaborators for their kindness of sending the lattice data in Ref. [21]. T.K. thanks Yuki Fujimoto and Larry McLerran for discussions on the quark saturation effects. The authors thank the Yukawa Institute for Theoretical Physics at Kyoto University and RIKEN iTHEMS. Discussions during the workshop (YITP-T-23-05) on "Condensed Matter Physics of QCD 2024" were useful to complete this work.

Conflicts of Interest: The authors declare no conflicts of interest.

Abbreviations

The following abbreviations are used in this manuscript:

QC_2D	two-color quantum chromodynamics
QCD_I	isospin QCD
EOS	equations of state
$\Lambda_{\rm QCD} \simeq 200$–$300$ MeV	non-perturbative scale in QCD
$n_0 \simeq 0.16\,{\rm fm}^{-3}$	nuclear saturation density
ChPT	Chiral perturbation theory

References

1. Kogut, J.B.; Stephanov, M.A.; Toublan, D. On two color QCD with baryon chemical potential. *Phys. Lett. B* **1999**, *464*, 183–191. [CrossRef]
2. Kogut, J.B.; Stephanov, M.A.; Toublan, D.; Verbaarschot, J.J.M.; Zhitnitsky, A. QCD-like theories at finite baryon density. *Nucl. Phys. B* **2000**, *582*, 477–513. [CrossRef]
3. Iida, K.; Itou, E.; Murakami, K.; Suenaga, D. Lattice study on finite density QC_2D towards zero temperature. *arXiv* **2024**, arXiv:2405.20566.
4. Iida, K.; Itou, E.; Lee, T.G. Two-colour QCD phases and the topology at low temperature and high density. *J. High Energy Phys.* **2020**, *1*, 181. [CrossRef]

5. Iida, K.; Itou, E.; Lee, T.G. Relative scale setting for two-color QCD with $N_f = 2$ Wilson fermions. *Prog. Theor. Exp. Phys.* **2021**, *2021*, 013B05. [CrossRef]
6. Boz, T.; Giudice, P.; Hands, S.; Skullerud, J.I. Dense two-color QCD towards continuum and chiral limits. *Phys. Rev. D* **2020**, *101*, 074506. [CrossRef]
7. Boz, T.; Cotter, S.; Fister, L.; Mehta, D.; Skullerud, J.I. Phase transitions and gluodynamics in 2-colour matter at high density. *Eur. Phys. J. A* **2013**, *49*, 87. [CrossRef]
8. Cotter, S.; Giudice, P.; Hands, S.; Skullerud, J.I. Towards the phase diagram of dense two-color matter. *Phys. Rev. D* **2013**, *87*, 034507. [CrossRef]
9. Hands, S.; Kenny, P.; Kim, S.; Skullerud, J.I. Lattice Study of Dense Matter with Two Colors and Four Flavors. *Eur. Phys. J. A* **2011**, *47*, 60. [CrossRef]
10. Astrakhantsev, N.; Braguta, V.; Ilgenfritz, E.; Kotov, A.; Nikolaev, A. Lattice study of thermodynamic properties of dense QC_2D. *Phys. Rev. D* **2020**, *102*, 074507. [CrossRef]
11. Bornyakov, V.G.; Braguta, V.V.; Nikolaev, A.A.; Rogalyov, R.N. Effects of Dense Quark Matter on Gluon Propagators in Lattice QC_2D. *Phys. Rev. D* **2020**, *102*, 114511. [CrossRef]
12. Muroya, S.; Nakamura, A.; Nonaka, C. Behavior of hadrons at finite density: Lattice study of color SU(2) QCD. *Phys. Lett. B* **2003**, *551*, 305–310. [CrossRef]
13. Suenaga, D.; Murakami, K.; Itou, E.; Iida, K. Probing the hadron mass spectrum in dense two-color QCD with the linear sigma model. *Phys. Rev. D* **2023**, *107*, 054001. [CrossRef]
14. Suenaga, D.; Murakami, K.; Itou, E.; Iida, K. Mass spectrum of spin-one hadrons in dense two-color QCD: Novel predictions by extended linear sigma model. *arXiv* **2023**, arXiv:2312.17017.
15. Kawaguchi, M.; Suenaga, D. Sound velocity peak induced by the chiral partner in dense two-color QCD. *arXiv* **2024**, arXiv:2402.00430.
16. Sun, G.f.; He, L.; Zhuang, P. BEC-BCS crossover in the Nambu-Jona-Lasinio model of QCD. *Phys. Rev. D* **2007**, *75*, 096004. [CrossRef]
17. Brauner, T.; Fukushima, K.; Hidaka, Y. Two-color quark matter: U(1)(A) restoration, superfluidity, and quarkyonic phase. *Phys. Rev. D* **2009**, *80*, 074035; Erratum in *Phys. Rev. D* **2010**, *81*, 119904. [CrossRef]
18. Strodthoff, N.; von Smekal, L. Polyakov-Quark-Meson-Diquark Model for two-color QCD. *Phys. Lett. B* **2014**, *731*, 350–357. [CrossRef]
19. Strodthoff, N.; Schaefer, B.J.; von Smekal, L. Quark-meson-diquark model for two-color QCD. *Phys. Rev. D* **2012**, *85*, 074007. [CrossRef]
20. Abbott, R.; Detmold, W.; Illa, M.; Parreño, A.; Perry, R.J.; Romero-López, F.; Shanahan, P.E.; Wagman, M.L. QCD constraints on isospin-dense matter and the nuclear equation of state. *arXiv* **2024**, arXiv:2406.09273.
21. Abbott, R.; Detmold, W.; Romero-López, F.; Davoudi, Z.; Illa, M.; Parreño, A.; Perry, R.J.; Shanahan, P.E.; Wagman, M.L. Lattice quantum chromodynamics at large isospin density: 6144 pions in a box. *arXiv* **2023**, arXiv:2307.15014.
22. Brandt, B.B.; Cuteri, F.; Endrodi, G. Equation of state and speed of sound of isospin-asymmetric QCD on the lattice. *J. High Energy Phys.* **2023**, *7*, 55, [CrossRef]
23. Son, D.T.; Stephanov, M.A. QCD at finite isospin density. *Phys. Rev. Lett.* **2001**, *86*, 592–595. [CrossRef]
24. Son, D.T.; Stephanov, M.A. QCD at finite isospin density: From pion to quark-antiquark condensation. *Phys. Atom. Nucl.* **2001**, *64*, 834–842. [CrossRef]
25. Splittorff, K.; Son, D.T.; Stephanov, M.A. QCD-like theories at finite baryon and isospin density. *Phys. Rev. D* **2001**, *64*, 016003. [CrossRef]
26. Gómez Nicola, A.; Vioque-Rodríguez, A. Effective Lagrangian at nonzero isospin chemical potential. *Phys. Rev. D* **2022**, *106*, 114017. [CrossRef]
27. Lu, Z.Y.; Xia, C.J.; Ruggieri, M. Thermodynamics and susceptibilities of isospin imbalanced QCD matter. *Eur. Phys. J. C* **2020**, *80*, 46. [CrossRef]
28. Fraga, E.S.; Palhares, L.F.; Villavicencio, C. Quark mass and isospin dependence of the deconfining critical temperature. *Phys. Rev. D* **2009**, *79*, 014021. [CrossRef]
29. Stiele, R.; Fraga, E.S.; Schaffner-Bielich, J. Thermodynamics of (2+1)-flavor strongly interacting matter at nonzero isospin. *Phys. Lett. B* **2014**, *729*, 72–78. [CrossRef]
30. Graf, T.; Schaffner-Bielich, J.; Fraga, E.S. Perturbative thermodynamics at nonzero isospin density for cold QCD. *Phys. Rev. D* **2016**, *93*, 085030. [CrossRef]
31. Brandt, B.B.; Endrodi, G.; Fraga, E.S.; Hippert, M.; Schaffner-Bielich, J.; Schmalzbauer, S. New class of compact stars: Pion stars. *Phys. Rev. D* **2018**, *98*, 094510. [CrossRef]
32. Fukushima, K.; Hatsuda, T. The phase diagram of dense QCD. *Rep. Prog. Phys.* **2011**, *74*, 014001. [CrossRef]
33. Oertel, M.; Hempel, M.; Klähn, T.; Typel, S. Equations of state for supernovae and compact stars. *Rev. Mod. Phys.* **2017**, *89*, 015007. [CrossRef]
34. Baym, G.; Hatsuda, T.; Kojo, T.; Powell, P.D.; Song, Y.; Takatsuka, T. From hadrons to quarks in neutron stars: A review. *Rep. Prog. Phys.* **2018**, *81*, 056902. [CrossRef]
35. Kojo, T. QCD equations of state and speed of sound in neutron stars. *AAPPS Bull.* **2021**, *31*, 11. [CrossRef]

36. Vuorinen, A. Particle-theory Input for Neutron-star Physics. *Acta Phys. Polon. B* **2024**, *55*, 4-A4. [CrossRef]
37. Drischler, C.; Han, S.; Lattimer, J.M.; Prakash, M.; Reddy, S.; Zhao, T. Limiting masses and radii of neutron stars and their implications. *Phys. Rev. C* **2021**, *103*, 045808. [CrossRef]
38. Han, M.Z.; Huang, Y.J.; Tang, S.P.; Fan, Y.Z. Plausible presence of new state in neutron stars with masses above $0.98M_{TOV}$. *Sci. Bull.* **2023**, *68*, 913–919. [CrossRef]
39. Kojo, T.; Baym, G.; Hatsuda, T. Implications of NICER for Neutron Star Matter: The QHC21 Equation of State. *Astrophys. J.* **2022**, *934*, 46. [CrossRef]
40. Huang, Y.J.; Baiotti, L.; Kojo, T.; Takami, K.; Sotani, H.; Togashi, H.; Hatsuda, T.; Nagataki, S.; Fan, Y.Z. Merger and Postmerger of Binary Neutron Stars with a Quark-Hadron Crossover Equation of State. *Phys. Rev. Lett.* **2022**, *129*, 181101. [CrossRef] [PubMed]
41. Fujimoto, Y.; Fukushima, K.; Hotokezaka, K.; Kyutoku, K. Gravitational Wave Signal for Quark Matter with Realistic Phase Transition. *Phys. Rev. Lett.* **2023**, *130*, 091404. [CrossRef] [PubMed]
42. Kedia, A.; Kim, H.I.; Suh, I.S.; Mathews, G.J. Binary neutron star mergers as a probe of quark-hadron crossover equations of state. *Phys. Rev. D* **2022**, *106*, 103027. [CrossRef]
43. Bauswein, A.; Bastian, N.U.F.; Blaschke, D.B.; Chatziioannou, K.; Clark, J.A.; Fischer, T.; Oertel, M. Identifying a first-order phase transition in neutron star mergers through gravitational waves. *Phys. Rev. Lett.* **2019**, *122*, 061102. [CrossRef] [PubMed]
44. McLerran, L.; Reddy, S. Quarkyonic Matter and Neutron Stars. *Phys. Rev. Lett.* **2019**, *122*, 122701. [CrossRef] [PubMed]
45. Jeong, K.S.; McLerran, L.; Sen, S. Dynamically generated momentum space shell structure of quarkyonic matter via an excluded volume model. *Phys. Rev. C* **2020**, *101*, 035201. [CrossRef]
46. Kojo, T. Stiffening of matter in quark-hadron continuity. *Phys. Rev. D* **2021**, *104*, 074005. [CrossRef]
47. Fujimoto, Y.; Kojo, T.; McLerran, L.D. Momentum Shell in Quarkyonic Matter from Explicit Duality: A Dual Model for Cold, Dense QCD. *Phys. Rev. Lett.* **2024**, *132*, 112701. [CrossRef]
48. Hayata, T.; Hidaka, Y.; Nishimura, K. Dense QCD_2 with matrix product states. *arXiv* **2023**, arXiv:2311.11643.
49. Mannarelli, M. Meson condensation. *Particles* **2019**, *2*, 411–443. [CrossRef]
50. Chiba, R.; Kojo, T. Sound velocity peak and conformality in isospin QCD. *Phys. Rev. D* **2024**, *109*, 076006. [CrossRef]
51. Chiba, R.; Kojo, T.; Suenaga, D. Thermal effects on sound velocity peak and conformality in isospin QCD. *arXiv* **2024**, arXiv:2403.02538.
52. Fujimoto, Y. Enhanced contribution of the pairing gap to the QCD equation of state at large isospin chemical potential. *Phys. Rev. D* **2024**, *109*, 054035. [CrossRef]
53. Cohen, T.D. QCD inequalities for the nucleon mass and the free energy of baryonic matter. *Phys. Rev. Lett.* **2003**, *91*, 032002. [CrossRef]
54. Navarrete, P.; Paatelainen, R.; Seppänen, K. Perturbative QCD meets phase quenching: The pressure of cold Quark Matter. *arXiv* **2024**, arXiv:2403.02180.
55. Fujimoto, Y.; Reddy, S. Bounds on the equation of state from QCD inequalities and lattice QCD. *Phys. Rev. D* **2024**, *109*, 014020. [CrossRef]
56. Moore, G.D.; Gorda, T. Bounding the QCD Equation of State with the Lattice. *J. High Energy Phys.* **2023**, *12*, 133. [CrossRef]
57. Adhikari, P.; Andersen, J.O.; Kneschke, P. On-shell parameter fixing in the quark-meson model. *Phys. Rev. D* **2017**, *95*, 036017. [CrossRef]
58. Ayala, A.; Bandyopadhyay, A.; Farias, R.L.S.; Hernández, L.A.; Hernández, J.L. QCD equation of state at finite isospin density from the linear sigma model with quarks: The cold case. *arXiv* **2023**, arXiv:2301.13633.
59. Gao, B.; Minamikawa, T.; Kojo, T.; Harada, M. Impacts of the U(1)A anomaly on nuclear and neutron star equation of state based on a parity doublet model. *Phys. Rev. C* **2022**, *106*, 065205. [CrossRef]
60. Minamikawa, T.; Gao, B.; Kojo, T.; Harada, M. Chiral restoration of nucleons in neutron star matter: Studies based on a parity doublet model. *arXiv* **2023**, arXiv:2302.00825.
61. Hatsuda, T.; Tachibana, M.; Yamamoto, N.; Baym, G. New critical point induced by the axial anomaly in dense QCD. *Phys. Rev. Lett.* **2006**, *97*, 122001. [CrossRef] [PubMed]
62. Yamamoto, N.; Tachibana, M.; Hatsuda, T.; Baym, G. Phase structure, collective modes, and the axial anomaly in dense QCD. *Phys. Rev. D* **2007**, *76*, 074001. [CrossRef]
63. Hatsuda, T.; Tachibana, M.; Yamamoto, N. Spectral Continuity in Dense QCD. *Phys. Rev. D* **2008**, *78*, 011501. [CrossRef]
64. Zhang, Z.; Fukushima, K.; Kunihiro, T. Number of the QCD critical points with neutral color superconductivity. *Phys. Rev. D* **2009**, *79*, 014004. [CrossRef]
65. Schäfer, T.; Wilczek, F. Continuity of quark and hadron matter. *Phys. Rev. Lett.* **1999**, *82*, 3956–3959. [CrossRef]
66. Masuda, K.; Hatsuda, T.; Takatsuka, T. Hadron-Quark Crossover and Massive Hybrid Stars with Strangeness. *Astrophys. J.* **2013**, *764*, 12. [CrossRef]
67. Masuda, K.; Hatsuda, T.; Takatsuka, T. Hadron–quark crossover and massive hybrid stars. *Prog. Theor. Exp. Phys.* **2013**, *2013*, 073D01. [CrossRef]
68. Masuda, K.; Hatsuda, T.; Takatsuka, T. Hyperon Puzzle, Hadron-Quark Crossover and Massive Neutron Stars. *Eur. Phys. J. A* **2016**, *52*, 65. [CrossRef]
69. Tajima, H.; Tsutsui, S.; Doi, T.M.; Iida, K. Density-Induced Hadron–Quark Crossover via the Formation of Cooper Triples. *Symmetry* **2023**, *15*, 333. [CrossRef]

70. Ma, Y.L.; Rho, M. Towards the hadron–quark continuity via a topology change in compact stars. *Prog. Part. Nucl. Phys.* **2020**, *113*, 103791. [CrossRef]
71. 't Hooft, G. A Planar Diagram Theory for Strong Interactions. *Nucl. Phys. B* **1974**, *72*, 461. [CrossRef]
72. Witten, E. Baryons in the 1/n Expansion. *Nucl. Phys. B* **1979**, *160*, 57–115. [CrossRef]
73. Nishimura, T.; Kitazawa, M.; Kunihiro, T. Anomalous enhancement of dilepton production as a precursor of color superconductivity. *Prog. Theor. Exp. Phys.* **2022**, *2022*, 093D02. [CrossRef]
74. Kitazawa, M.; Koide, T.; Kunihiro, T.; Nemoto, Y. Pre-critical phenomena of two-flavor color superconductivity in heated quark matter: Diquark-pair fluctuations and non-Fermi liquid behavior. *Prog. Theor. Phys.* **2005**, *114*, 117–155. [CrossRef]
75. Kitazawa, M.; Koide, T.; Kunihiro, T.; Nemoto, Y. Precursor of color superconductivity in hot quark matter. *Phys. Rev. D* **2002**, *65*, 091504. [CrossRef]
76. Blaschke, D.; Buballa, M.; Dubinin, A.; Roepke, G.; Zablocki, D. Generalized Beth–Uhlenbeck approach to mesons and diquarks in hot, dense quark matter. *Ann. Phys.* **2014**, *348*, 228–255. [CrossRef]
77. Boz, T.; Hajizadeh, O.; Maas, A.; Skullerud, J.I. Finite-density gauge correlation functions in QC2D. *Phys. Rev. D* **2019**, *99*, 074514. [CrossRef]
78. Kojo, T.; Baym, G. Color screening in cold quark matter. *Phys. Rev. D* **2014**, *89*, 125008. [CrossRef]
79. Suenaga, D.; Kojo, T. Gluon propagator in two-color dense QCD: Massive Yang-Mills approach at one-loop. *Phys. Rev. D* **2019**, *100*, 076017. [CrossRef]
80. Kojo, T.; Suenaga, D. Thermal quarks and gluon propagators in two-color dense QCD. *Phys. Rev. D* **2021**, *103*, 094008. [CrossRef]
81. Contant, R.; Huber, M.Q. Dense two-color QCD from Dyson-Schwinger equations. *Phys. Rev. D* **2020**, *101*, 014016. [CrossRef]
82. Kojo, T.; Hidaka, Y.; McLerran, L.; Pisarski, R.D. Quarkyonic Chiral Spirals. *Nucl. Phys. A* **2010**, *843*, 37–58. [CrossRef]
83. Kojo, T.; Pisarski, R.D.; Tsvelik, A.M. Covering the Fermi Surface with Patches of Quarkyonic Chiral Spirals. *Phys. Rev. D* **2010**, *82*, 074015. [CrossRef]
84. Kojo, T.; Hidaka, Y.; Fukushima, K.; McLerran, L.D.; Pisarski, R.D. Interweaving Chiral Spirals. *Nucl. Phys. A* **2012**, *875*, 94–138. [CrossRef]
85. Kojo, T.; Su, N. The quark mass gap in a magnetic field. *Phys. Lett. B* **2013**, *720*, 192–197. [CrossRef]
86. Kojo, T.; Su, N. The quark mass gap in strong magnetic fields. *Nucl. Phys. A* **2014**, *931*, 763–768. [CrossRef]
87. Hattori, K.; Kojo, T.; Su, N. Mesons in strong magnetic fields: (I) General analyses. *Nucl. Phys. A* **2016**, *951*, 1–30. [CrossRef]
88. Novikov, V.A.; Okun, L.B.; Shifman, M.A.; Vainshtein, A.I.; Voloshin, M.B.; Zakharov, V.I. Charmonium and Gluons: Basic Experimental Facts and Theoretical Introduction. *Phys. Rep.* **1978**, *41*, 1–133. [CrossRef]
89. Shifman, M.A.; Vainshtein, A.I.; Zakharov, V.I. QCD and Resonance Physics. Theoretical Foundations. *Nucl. Phys. B* **1979**, *147*, 385–447. [CrossRef]
90. Shifman, M.A.; Vainshtein, A.I.; Zakharov, V.I. QCD and Resonance Physics: Applications. *Nucl. Phys. B* **1979**, *147*, 448–518. [CrossRef]
91. Lee, T.D.; Yang, C.N. Charge Conjugation, a New Quantum Number *G*, and Selection Rules Concerning a Nucleon Anti-nucleon System. *Nuovo Cim.* **1956**, *10*, 749–753. [CrossRef]
92. Andersen, J.O.; Adhikari, P.; Kneschke, P. Pion condensation and QCD phase diagram at finite isospin density. *Proc. Sci.* **2019**, *336*, 197. [CrossRef]
93. Coleman, S.R.; Weinberg, E.J. Radiative Corrections as the Origin of Spontaneous Symmetry Breaking. *Phys. Rev. D* **1973**, *7*, 1888–1910. [CrossRef]
94. Duarte, D.C.; Hernandez-Ortiz, S.; Jeong, K.S.; McLerran, L.D. Quarkyonic effective field theory, quark-nucleon duality, and ghosts. *Phys. Rev. D* **2021**, *104*, L091901. [CrossRef]
95. Hatsuda, T.; Kunihiro, T. QCD phenomenology based on a chiral effective Lagrangian. *Phys. Rep.* **1994**, *247*, 221–367. [CrossRef]
96. Tanabashi, M. et al. [Particle Data Group] Review of Particle Physics. *Phys. Rev. D* **2018**, *98*, 030001. [CrossRef]
97. Ananthanarayan, B.; Caprini, I.; Das, D. Electromagnetic charge radius of the pion at high precision. *Phys. Rev. Lett.* **2017**, *119*, 132002. [CrossRef]
98. Koponen, J.; Bursa, F.; Davies, C.T.H.; Dowdall, R.J.; Lepage, G.P. Size of the pion from full lattice QCD with physical u, d, s and c quarks. *Phys. Rev. D* **2016**, *93*, 054503. [CrossRef]
99. Wang, G.; Liang, J.; Draper, T.; Liu, K.F.; Yang, Y.B. Lattice Calculation of Pion Form Factor with Overlap Fermions. *Phys. Rev. D* **2021**, *104*, 074502. [CrossRef]
100. Polyakov, M.V. Generalized parton distributions and strong forces inside nucleons and nuclei. *Phys. Lett. B* **2003**, *555*, 57–62. [CrossRef]
101. Kharzeev, D.E. Mass radius of the proton. *Phys. Rev. D* **2021**, *104*, 054015. [CrossRef]
102. Kaiser, N.; Weise, W. Sizes of the Nucleon. *arXiv* **2024**, arXiv:2404.11292.
103. Fujimoto, Y.; Fukushima, K.; McLerran, L.D.; Praszalowicz, M. Trace Anomaly as Signature of Conformality in Neutron Stars. *Phys. Rev. Lett.* **2022**, *129*, 252702. [CrossRef]
104. Marczenko, M.; McLerran, L.; Redlich, K.; Sasaki, C. Reaching percolation and conformal limits in neutron stars. *arXiv* **2022**, arXiv:2207.13059.
105. Tajima, H.; Iida, K.; Liang, H. Nonrelativistic trace anomaly and equation of state in dense fermionic matter. *Phys. Rev. C* **2024**, *109*, 055203. [CrossRef]

106. Kojo, T.; Powell, P.D.; Song, Y.; Baym, G. Phenomenological QCD equation of state for massive neutron stars. *Phys. Rev. D* **2015**, *91*, 045003. [CrossRef]
107. Kojo, T.; Suenaga, D. Peaks of sound velocity in two color dense QCD: Quark saturation effects and semishort range correlations. *Phys. Rev. D* **2022**, *105*, 076001. [CrossRef]
108. Geißel, A.; Gorda, T.; Braun, J. Pressure and speed of sound in two-flavor color-superconducting quark matter at next-to-leading order. *arXiv* **2024**, arXiv:2403.18010.
109. Braun, J.; Geißel, A.; Schallmo, B. Speed of sound in dense strong-interaction matter. *SciPost Phys. Core* **2024**, *7*, 015. [CrossRef]
110. Leonhardt, M.; Pospiech, M.; Schallmo, B.; Braun, J.; Drischler, C.; Hebeler, K.; Schwenk, A. Symmetric nuclear matter from the strong interaction. *Phys. Rev. Lett.* **2020**, *125*, 142502. [CrossRef]
111. Fukushima, K.; Kojo, T.; Weise, W. Hard-core deconfinement and soft-surface delocalization from nuclear to quark matter. *Phys. Rev. D* **2020**, *102*, 096017. [CrossRef]
112. Saito, K.; Tsushima, K.; Thomas, A.W. Nucleon and hadron structure changes in the nuclear medium and impact on observables. *Prog. Part. Nucl. Phys.* **2007**, *58*, 1–167. [CrossRef]
113. Geesaman, D.F.; Saito, K.; Thomas, A.W. The nuclear EMC effect. *Ann. Rev. Nucl. Part. Sci.* **1995**, *45*, 337–390. [CrossRef]
114. Koch, V.; McLerran, L.; Miller, G.A.; Vovchenko, V. Might Normal Nuclear Matter be Quarkyonic? *arXiv* **2024**, arXiv:2403.15375.
115. McLerran, L.; Miller, G.A. The Quark Pauli Principle and the Transmutation of Nuclear Matter. *arXiv* **2024**, arXiv:2405.11074.
116. McLerran, L.; Pisarski, R.D. Phases of cold, dense quarks at large N(c). *Nucl. Phys. A* **2007**, *796*, 83–100. [CrossRef]